

INDUCED TURBULENCE AND THE DENSITY STRUCTURE OF THE DUST LAYER IN A PROTOPLANETARY DISK

TAKU TAKEUCHI¹, TAKAYUKI MUTO¹, SATOSHI OKUZUMI², NAOKI ISHITSU³, AND SHIGERU IDA¹

Accepted by the Astrophysical Journal

ABSTRACT

We study the turbulence induced in the dust layer of a protoplanetary disk based on the energetics of dust accretion due to gas drag. We estimate turbulence strength from the energy supplied by dust accretion, using the radial drift velocity of the dust particles in a laminar disk. Our estimate of the turbulence strength agrees with previous analytical and numerical research on the turbulence induced by Kelvin-Helmholtz and/or streaming instabilities for particles whose stopping time is less than the Keplerian time. For such small particles, the strongest turbulence is expected to occur when the dust-to-gas ratio of the disk is $\sim C_{\text{eff}}^{1/2}(h_g/r) \sim 10^{-2}$, where $C_{\text{eff}} \approx 0.2$ represents the energy supply efficiency to turbulence and $h_g/r \sim 5 \times 10^{-2}$ is the aspect ratio of the gas disk. The maximum viscosity parameter is $\alpha_{\text{max}} \sim C_{\text{eff}} T_s (h_g/r)^2 \sim 10^{-4} T_s$, where $T_s (< 1)$ is the non-dimensional stopping time of the dust particles. Modification in the dust-to-gas ratio from the standard value, 10^{-2} , by any process, results in weaker turbulence and a thinner dust layer, and consequently may accelerate the growth process of the dust particles.

Subject headings: accretion disks — planets and satellites: formation — protoplanetary disks

1. INTRODUCTION

The first step of planet formation in protoplanetary disks is the collisional growth of (sub-)micron-sized dust particles (or aggregates), and consequent sedimentation. Dust settling and the formation of a dust layer at the midplane of the disk play an important role in the subsequent planetesimal formation process. Enhancement of the particle density in the dust layer accelerates the collisional growth rate. If the density enhancement is high enough, planetesimals may form through the gravitational instability of the dust layer (Goldreich & Ward 1973; Sekiya 1983). However, the turbulent motion of the gas hinders the dust layer from thinning. Dust particles are stirred by turbulence and diffuse to high altitudes from the midplane. Thus, turbulence is an impediment to planetesimal formation. Turbulence excited by magneto-rotational instability (MRI) is so strong that the dust layer cannot become thin enough to induce planetesimal formation through gravitational instability (Johansen & Klahr 2005; Fromang & Papaloizou 2006; Turner et al. 2006; Carballido et al. 2006, 2011; Fromang & Nelson 2009). In addition, the turbulence-induced collisional velocity can be high enough to destroy dust aggregates (Carballido et al. 2008, 2010), though several mechanisms have been proposed to overcome this difficulty (Johansen et al. 2007, 2011; Lyra et al. 2008, 2009). Even if the gas disk exhibits an initially laminar flow (such as is expected in the dead zone where the ionization fraction of the gas is too low to couple to the magnetic field, as mentioned in Gammie 1996 and Sano et al.

2000), dust settling itself induces turbulence. The dust particles tend to rotate around the central star faster than the gas because the gas experiences a pressure gradient force acting in the opposite direction of the gravity of the star. When the dust layer thins and the dust-to-gas ratio in the layer approaches unity, the velocity difference from that of the upper gas layer induces Kelvin-Helmholtz (KH) instability and excites turbulence in the dust layer (e.g., Goldreich & Ward 1973; Sekiya & Ishitsu 2000, 2001; Garaud & Lin 2004). The velocity difference between the dust particles and the gas inside the dust layer also induces streaming instability (Youdin & Goodman 2005; Youdin & Johansen 2007; Johansen & Youdin 2007; see Chiang & Youdin 2010 for review on the various instability in the dust layer). Laminar gas disks are considered excellent sites for planetesimal formation. Thus, it is important to clarify how turbulence induced in the dust layer diffuses the dust particles, versus dust sedimentation. Several analytical and numerical studies have focused on this problem (Cuzzi et al. 1993; Champney et al. 1995; Sekiya 1998; Dobrovolskis et al. 1999; Johansen et al. 2006; Michikoshi & Inutsuka 2006; Weidenschilling 2006, 2010; Bai & Stone 2010a, 2010b).

Sekiya (1998, hereafter S98) analytically solved for the structure of the dust layer under turbulence induced by KH instability. To derive the density profile of the dust layer analytically, the author adopted several assumptions. First, the dust particles were assumed to be small enough and were coupled so tightly to the gas that the dust and the gas could be treated as a single fluid. Second, the density structure was adjusted to keep the dust layer marginally unstable to KH instability. Third, the effects of the Coriolis force and of the Keplerian shear were neglected. These assumptions allowed the author to determine analytically the density structure of the dust layer and to discuss how far from the midplane the dust particles diffuse due to turbulence. The analysis in S98

¹Department of Earth and Planetary Sciences, Tokyo Institute of Technology, Meguro-ku, Tokyo, 152-8551, Japan; taku@geo.titech.ac.jp

²Department of Physics, Nagoya University, Nagoya, Aichi 464-8602, Japan

³National Astronomical Observatory, Mitaka, Tokyo 181-8588, Japan

provided a useful guide for subsequent numerical studies that investigated turbulence of the dust layer with more realistic assumptions. In reality, however, dust particles that are not tightly coupled to gas play an important role in inducing turbulence. Also, other kinds of instability, such as streaming instability, may occur before KH instability sets in (Bai & Stone 2010a). Thus, in addition to performing numerical simulations, it is desirable to include an analytic discussion on the structure of the dust layer using a more general set of assumptions than adopted in S98.

In this paper, we revisit the analysis presented in S98 from a different point of view. In S98, the density structure of the dust layer was determined by the condition that the dust layer was marginally unstable to KH instability; i.e., the Richardson number, Ri , had a constant critical value. In the stability condition on Ri , the free energy due to the shear velocity is compared with the energy needed to lift the material against the vertical gravity (Chandrasekhar 1961). In the case of a dust layer, the free energy of the azimuthal velocity is compared with the gravitational potential in the vertical direction. We also discuss the energetics of the dust layer to determine the density structure, but in this paper we focus on the gravitational potential in the radial direction. Sustaining steady turbulence requires an energy supply. The source of the free energy for KH instability or streaming instability is the velocity difference between the dust and the gas. Because this free energy is consumed in the process of exciting turbulence, a velocity difference must be continually induced to provide steady turbulence. This velocity difference originates from the force balance in the radial direction between the stellar gravity, the centrifugal force, and the pressure gradient. In other words, the velocity difference is induced because the gas resides in a slightly shallower effective potential (including both the stellar gravity and the gas pressure), than the effective potential for the dust. The dust loses its angular momentum due to gas drag and drifts towards the star, while the gas gains angular momentum and drifts outward. The total angular momentum remains constant. Because the effective potential for the dust is deeper, this process releases gravitational energy that can be a source of the free energy for turbulence. (The relationship between the angular momentum variation, ΔL , and the energy variation, ΔE , for circular orbiting material is $\Delta E = \Omega \Delta L$, where the angular velocity, Ω , is different for the gas and for the dust.) If the gas disk is initially in a state of laminar flow, i.e., if gas drag is the only process that exchanges angular momentum, then dust accretion is the source of the free energy used to induce turbulence. The accretion rate of the dust due to gas drag has been calculated in the literature (Nakagawa et al. 1986, hereafter NSH86; Weidenschilling 2003; Youdin & Chiang 2004). Using this dust accretion rate, and assuming that a certain fraction of the accretion energy is transferred to turbulence, it is straightforward to calculate the strength of the turbulence and to determine the density structure of the dust layer. In this paper, we show that an analysis of the energetics based on the gravitational potential in the radial direction results in a dust layer structure that is qualitatively equivalent to the dust layer structure developed in the analysis presented in S98. Most of the important properties of the S98 model are repro-

duced. Our analysis avoids some of the assumptions that were adopted in S98. Specifically, we do not assume tight coupling between the gas and the dust, nor a marginally unstable structure for KH instability. (The effects of the Coriolis force and of Keplerian shear, which are still neglected in this paper, are discussed by Ishitsu & Sekiya 2002, 2003; Gómez & Ostriker 2005; Chiang 2008; Barranco 2009; Lee et al. 2010.) Thus, the results of this paper may be applied to more general situations, including situations in which the dust is weakly coupled to the gas, or in which streaming instability acts as a source of turbulence.

In §2, we describe our model assumptions. In §3, the energy release rate of the accreting dust is calculated. In §4, the strength of the turbulence is derived and its asymptotic forms in the limits of a small dust-to-gas ratio and a tight dust-gas coupling are discussed. In §5, the results of our model are compared with the S98 model and with previous numerical simulations of KH instability and streaming instability. In §6.1, we discuss how dust layer formation reduces the radial drift velocity of the dust and the relative velocity of the dust particles. In §6.3, we check the applicability of our model to turbulence in the dust layer for the KH instability and streaming instability cases.

2. DISK MODEL AND ASSUMPTIONS

2.1. *Brief Model Description*

We consider a dust layer that forms after dust particles have settled to the midplane of a gas disk around a star. Before the dust settles, the gas disk is assumed to be subject to laminar flow. This means that we consider the dead zone where MRI is inactive because of the low degree of ionization. Turbulent gas motion may be present even in the dead zone because sound waves propagate from the active layers at high altitudes and disturb the gas in the dead zone (Fleming & Stone 2003; Suzuki et al. 2010; Okuzumi & Hirose 2011). We assume that the dead zone is wide enough that the active layer cannot induce strong turbulence at the midplane.

Even in an initially laminar disk, dust sedimentation and the formation of the midplane dust layer cannot proceed in a perfectly undisturbed fashion. When the midplane dust-to-gas ratio reaches a critical value, the velocity differences between the dust layer and the upper gas layer, or between the individual dust particles and the surrounding gas, will start to induce hydrodynamical instabilities, such as KH instability or streaming instability (see Chiang & Youdin 2010 for review). Consequently, turbulent diffusion of the dust particles terminates further dust settling. It is expected that a steady dust layer forms, in which particle settling and turbulent diffusion balance each other. In such a state, vertical settling is no longer an energy source for turbulence, but the radial accretion of the dust still proceeds. The turbulence is maintained by the energy liberated from dust accretion to the star.

We calculate the dust accretion rate and consequent energy release, assuming that a steady dust layer has formed. The strength of the turbulence is then estimated. The balance between the turbulent diffusion and the dust settling determines the dust layer thickness. Thus, the structure of the dust layer, the dust accretion

rate, and the turbulence strength must be determined self-consistently.

For simplicity, we focus on a narrow axisymmetric ring region at a certain radius r from the central star. We consider the dust layer structure only in the vertical direction, neglecting any radial variation in the properties of the gas disk and the dust layer. All the dust particles are assumed to have a uniform size, i.e., the size distribution of the dust particles is neglected in this paper.

2.2. Vertical Structure of the Dust Layer

If the effect of gas drag on the dust were negligible, the dust particles would orbit at the Keplerian velocity $\Omega_K = \sqrt{(GM)/r^3}$, where G is the gravitational constant and M is the mass of the central star. However, the orbital velocity of the gas is slightly less than the Keplerian velocity because the direction of the gas pressure gradient is usually outward from the star. This cancels part of the contribution to the orbital velocity from the gravity of the star. Given a negligible influence of the drag force from the dust, the angular velocity of the gas would be

$$\Omega_g = \sqrt{\frac{GM}{r^3}}(1 - 2\eta) \approx \Omega_K(1 - \eta). \quad (1)$$

Here, η represents the deviation of the gas orbital velocity from the Keplerian value. It is half of the ratio between the gas pressure gradient force and the gravity of the central star,

$$\eta = -\frac{1}{2\rho_g r \Omega_K^2} \frac{\partial P}{\partial r}, \quad (2)$$

where ρ_g and P are the gas density and pressure, respectively.

We consider a thin dust layer in which most of the dust particles have settled on the midplane of the gas disk. The gas disk is isothermal in the vertical direction with a scale height of $h_g = c_s/\Omega_K$, where c_s is the gas sound speed. Because the thickness of the dust layer is much smaller than the scale height of the gas disk, the gas density ρ_g in the dust layer is treated as a constant. Its value is given by the column density of the gas disk Σ_g as

$$\rho_g = \frac{\Sigma_g}{\sqrt{2\pi}h_g}. \quad (3)$$

The dust density profile in the vertical direction, $\rho_d(z)$, is determined by the balance between the dust settling and turbulent diffusion (Youdin & Lithwick 2007, hereafter YL07)⁴. The dust particles have a stopping time, $\tau_{\text{stop}} = T_s \Omega_K^{-1}$, in which the velocity difference from the background gas flow becomes $1/e$ times due to gas drag, where T_s is the non-dimensional stopping time. In a turbulent gas disk with a turbulent diffusion coefficient D_g , the density profile of the dust layer composed of

single-sized particles is Gaussian, $\rho_d = \rho_{d,0} \exp(-\tilde{z}^2)$, where $\tilde{z} = z/(\sqrt{2}h_d)$ is the non-dimensional vertical coordinate normalized by the dust scale height $h_d \approx [D_g/(\Omega_K T_s)]^{1/2}$. Note that the turbulent diffusion coefficient in the “z-direction”, D_g , may have a significantly different value from the usual turbulent viscosity coefficient ν_{acc} in accretion disks, where ν_{acc} comes from the “ $r\theta$ -component” of the Reynolds stress (e.g., Lesur & Ogilvie 2010). Nevertheless, we follow the conventional “ α -prescription”, and express the diffusion coefficient as $D_g = \alpha c_g h_g$ for simplicity. This prescription and equation (24) of YL07 give

$$h_d = \sqrt{\frac{\alpha}{T_s}} \sqrt{\frac{1 + T_s}{1 + 2T_s}} h_g. \quad (4)$$

The dust density profile is written as

$$\rho_d = f_{\text{mid}} \rho_g \exp(-\tilde{z}^2), \quad (5)$$

where the midplane dust-to-gas ratio f_{mid} is increased by a factor h_g/h_d from the total dust-to-gas ratio or the “metallicity” of the disk $Z_{\text{disk}} = \Sigma_d/\Sigma_g$,

$$f_{\text{mid}} = Z_{\text{disk}} \frac{h_g}{h_d} = Z_{\text{disk}} \sqrt{\frac{T_s}{\alpha}} \sqrt{\frac{1 + 2T_s}{1 + T_s}}. \quad (6)$$

We define $\beta(\tilde{z})$ as the ratio of the total (dust and gas) density to the gas density,

$$\beta = \frac{\rho_g + \rho_d}{\rho_g} = 1 + f_{\text{mid}} \exp(-\tilde{z}^2). \quad (7)$$

2.3. Typical Values of the Model Parameters

In our model, the turbulent parameter α and the structure of the dust layer (i.e., the thickness, h_d , and the midplane dust-to-gas ratio, f_{mid}) are determined for a given parameter set (the stopping time of the dust particles T_s , the disk metallicity Z_{disk} , and the parameters for the gas disk). The non-dimensional variables of the result (α , h_d/r , and f_{mid}) depend on the gas disk parameters only through

$$\tilde{\eta} = \eta^2 \left(\frac{r}{h_g} \right)^2, \quad (8)$$

where $\tilde{\eta} \sim \eta \sim (h_g/r)^2 \sim 10^{-3} - 10^{-2}$. The numerical calculations in the subsequent sections mainly use a value $\tilde{\eta} = (0.05/\gamma)^2 = 9 \times 10^{-4}$, where $\gamma = 5/3$, in order to compare our model with the simulation presented by Johansen et al. (2006, hereafter JHK06). In §5.2.2, $\tilde{\eta} = 0.05^2$ is used for comparison with the results by Bai & Stone (2010), and in §6.1, $\tilde{\eta} = 2.92 \times 10^{-3}$ is used to calculate the radial drift velocity of the dust in the gas disk model by Hayashi (1981). The $\tilde{\eta}$ dependence of the results will be discussed in §6.2.

3. TURBULENCE ENERGY SUPPLY

The energy supply for turbulence comes from liberation of the gravitational energy of the dust. As the dust falls towards the central star, the dust particles penetrate more deeply into the potential well of the star. Although the gas drifts outward to conserve the total angular momentum, the difference in the effective gravitational potential between the dust ($-GM/r$) and the

⁴ Note that the diffusion coefficient given by YL07 is derived assuming that the dust particles can be treated as passive particles. Problems may arise if this formula is used in a case where the dust layer is so dense that its dust-to-gas ratio is larger than unity. Although a comparison of our model with the simulation by Johansen et al. (2006) shows good agreement even for a dust-to-gas ratio as large as 40 (see Fig. 7), modeling the effect of the dust inertia will be a subject for future investigation using a refinement of the present model.

gas ($-GM(1 - 2\eta)/r$), including the work done by the pressure gradient, causes a net energy liberation. Part of the liberated energy is converted directly into thermal energy, and part is used for supplying energy to the turbulence (see discussion in §6.3).

Dust particle accretion occurs either individually or collectively. Individual dust particles suffer gas drag given a velocity difference between the particle and the gas. Usually the orbital velocity of the gas is slower than that of the dust particle, and the gas drag force decelerates the particle orbital motion. Thus, the particle loses its angular momentum and drifts inward. In addition to this individual drift, a collective drag works on the whole dust layer. The dust layer at the midplane orbits faster than the gas layer at higher altitudes because in the dust layer the increased inertia of the enriched dust particles weakens the effect of the gas pressure. The dust layer rotates with a velocity close to the Keplerian value. The upper gas layer, devoid of the inertia of the dust, orbits more slowly than the midplane dust layer. If the gas exhibits turbulent viscosity, then the slower orbiting gas layer exerts a drag force on the dust layer, and consequently the dust layer loses its angular momentum and accretes inward. We consider the energy release rate of the dust caused by individual and collective drag.

3.1. Dust Accretion Caused by Individual Drag

We calculate the gravitational energy released when dust particles accrete towards the star due to drag on individual particles. In this calculation, we assume that the gas disk is in a laminar flow state, and that dust particles drift inward steadily. Any random motion of particles caused by gas turbulence is neglected. We expect that in turbulent gas disks, the average motion of the dust particles can be estimated from the motion in the laminar disk (Bai & Stone 2010). Because the individual drag is more effective than the collective drag when the midplane dust-to-gas ratio is less than unity (see Fig. 1 below), we take the $f_{\text{mid}} \ll 1$ limit in the following calculation. The calculation for a general f_{mid} is described in Appendix B.

In a laminar disk, the particle drift velocity $v_{d,r}$ is given by equation (2.11) of NSH86. For $\rho_d \ll \rho_g$, the particle radial velocity is (see also eq. [23] of Takeuchi & Lin (2002); note the factor of 2 difference in the definition of η)

$$v_{d,r} = -\frac{2T_s}{T_s^2 + 1}\eta v_K. \quad (9)$$

The gas drifts in the opposite direction with a velocity $v_{g,r}$. From angular momentum conservation, the gas drift velocity is

$$v_{g,r} = -\frac{\rho_d}{\rho_g}v_{d,r}. \quad (10)$$

The effective gravities (including the pressure gradient force) acting on the dust and on the gas are $g_d = -GM/r^2 = -r\Omega_K^2$ and $g_g = -GM(1 - 2\eta)/r^2 = -r\Omega_g^2$, respectively. While the total angular momentum is conserved, the total energy is not conserved because of the difference in the effective gravities acting on the gas and on the dust, $\rho_d g_d v_{d,r} + \rho_g g_g v_{g,r} \neq 0$, providing a source of energy for turbulence.

Note that, in the above calculation, $v_{d,r}$ and $v_{g,r}$ are the “terminal velocities”. This means that the gravitational accelerations of the dust and gas are balanced by the drag forces, and liberated energy translates directly into thermal energy. Thus, no energy would be contributed to turbulence. In reality, however, if the gas disk is turbulent, a steady terminal velocity is not expected, and acceleration phases of the dust must occur, as discussed in §6.3. In an acceleration phase, the work done by gravity first provides kinetic energy, which can be translated into turbulent energy. We estimate this energy input to turbulence. In the following calculation, the energy liberated from the accreting dust is estimated using the terminal velocity described above for simplicity. Only a certain fraction of the liberated energy goes into turbulence. Thus, the energy input to turbulence is a factor $C_{\text{eff}} (< 1)$ times the following estimation. The factor C_{eff} will be determined in §5.2 to be ≈ 0.2 by comparing our model with the numerical simulation of turbulence in the dust layer developed by JHK06.

Given that some portion of the accretion energy of the dust is consumed by the outward motion of the gas, the liberated gravitational energy per unit surface area of the disk is,

$$\frac{\partial E_{\text{drag}}}{\partial t} = \frac{1}{2} \int_{-\infty}^{\infty} (\rho_d g_d v_{d,r} + \rho_g g_g v_{g,r}) dz, \quad (11)$$

where the factor of 1/2 comes from the fact that half of the work done by gravity is used for acceleration (and deceleration) of the azimuthal velocity of the dust (and of the gas) as their semi-major axes change. Using equation (9) and (10), the energy liberation rate reduces to

$$\frac{\partial E_{\text{drag}}}{\partial t} = 2\eta^2 v_K^2 \Omega_K T_s \Sigma_{d,\text{drag}}, \quad (12)$$

where the effective “surface density” $\Sigma_{d,\text{drag}}$ of the dust is

$$\Sigma_{d,\text{drag}} = \frac{1}{T_s^2 + 1} \Sigma_d. \quad (13)$$

In the above calculation, we assume $f_{\text{mid}} \ll 1$. The calculation of the energy liberation rate for general f_{mid} is described in Appendix B. In the numerical calculations in the subsequent sections, we use equation (B5) for the effective surface density⁵,

$$\Sigma_{d,\text{drag}} = \frac{\Sigma_d}{\sqrt{\pi}} \int_{-\infty}^{\infty} \frac{\exp(-\tilde{z}^2)}{T_s^2 + \beta^2} \left[1 - \frac{T_s^2}{2(T_s^2 + \beta^2)} \right] d\tilde{z}. \quad (14)$$

If the dust particles are tightly coupled to the gas ($T_s \ll 1$) and dust sedimentation is weak ($f_{\text{mid}} \ll 1$), then $\Sigma_{d,\text{drag}}$ is simply equal to the dust surface density Σ_d .

3.2. Dust Accretion Caused by Collective Drag

Next, we consider dust accretion due to collective drag acting on the entire dust layer. Because the faster-orbiting dust particles drag the gas in the dust layer, the

⁵ Equation (14) does not coincide with equation (13) in the limit of $f_{\text{mid}} \ll 1$. This discrepancy comes from the fact that the calculation of equation (14) includes correction terms of the order of η^2 in the drift velocity, while equation (13) considers only the terms of η . The difference between equations (13) and (14) is at most factor 2 (for $T_s \gg 1$), and is not significant.

orbital velocity of the gas is largest at the midplane and decreases with altitude. If the gas in the dust layer is turbulent, the variation in orbital velocity $v_{g,\theta}$ with altitude z induces Reynolds stress $P_{\theta z}$. This causes a transfer of angular momentum from the dust layer to the upper gas layer, resulting in accretion of the dust layer.

To calculate the energy liberation rate, we make a few key assumptions. First, we consider only the θz -component of the Reynolds stress, $P_{\theta z}$, neglecting the other components $P_{r\theta}$ and P_{zr} . Ignoring $P_{r\theta}$ means that turbulence in the dust layer does not transfer the angular momentum efficiently in the radial direction. This is expected for turbulence induced by hydrodynamical instabilities such as convective instability (e.g., Stone & Balbus 1996; Lesur & Ogilvie 2010). The Reynolds stress P_{zr} is also neglected for simplicity. Brauer et al. (2007) pointed out that P_{zr} changes the velocity profiles of the dust and gas from those derived by NSH86 by a factor ~ 3 , and thus P_{zr} cannot be neglected in a rigorous discussion. Obtaining the exact velocity profiles including P_{zr} requires numerical calculations. In this paper, we use the velocity profiles calculated analytically by NSH86 for simplicity. This induces an error of a factor ~ 3 in our estimation of turbulence strength. Thus, our estimate is limited to an order-of-magnitude argument.

The second assumption is that the turbulent layer has a thickness comparable to that of the dust layer. If the turbulent layer were much thicker than the dust layer and most of the volume of the turbulent layer were free of the dust, then its structure would be controlled by the gas, unaffected by the properties of the dust and the structure of the dust layer. The dust layer would behave just like a boundary wall at the bottom of the turbulent layer. Turbulence in such a thick boundary gas layer has been discussed using the analogy of the Ekman layer (e.g., Cuzzi et al. 1993). If the turbulent layer were dominated by the dust layer, then the structure of the dust layer would control the turbulence strength. We focus on such a dusty turbulent layer. Following Youdin & Chiang (2004), we consider the conditions needed for the turbulent and dust layers to be of similar thickness. The thickness of the turbulent layer, from dimensional analysis, is the Ekman length,

$$h_E \sim \sqrt{\frac{\nu}{\Omega_K}}, \quad (15)$$

where ν is the turbulent viscosity, provided that the viscosity and the Coriolis force determine the layer structure. The thickness of the dust layer (eq. [4]), which is determined by the balance between sedimentation and diffusion of the dust particles, is

$$h_d \sim \sqrt{\frac{\nu}{T_s \Omega_K}}, \quad (16)$$

where $\nu \sim D_g$ is used. For small particles ($T_s \lesssim 1$), h_d is larger than h_E , meaning that such small particles move further out of the turbulent layer and modify the structure of the turbulent layer. It is expected that the thickness of the turbulent layer is not given by h_E , but by h_d (see also S98; Goodman & Pindor 2000). For large particles ($T_s \gg 1$), the turbulent layer is much thicker than the dust layer, and its thickness is expected to be h_E . In the following discussion, we consider a dusty tur-

bulent layer with a thickness similar to h_d . Thus, the analysis in this paper is probably not appropriate for large particles ($T_s \gg 1$).

Under the above assumptions, the energy liberation rate is estimated. Because the collective drag is effective only if the midplane dust-to-gas ratio is larger than unity (see Fig. 1 below), we consider the case in which a dense dust layer has formed ($f_{\text{mid}} \gtrsim 1$) and use the plate drag approximation (Goldreich & Ward 1973; Goodman & Pindor 2000; Weidenschilling 2003). The calculation for general f_{mid} is described in Appendix C. The Reynolds stress $P_{\theta z}$ near the boundary between the dust layer (or the turbulent layer) and the gas layer is estimated as

$$P_{\theta z} = \rho_g \nu \frac{\partial v_{g,\theta}}{\partial z} \sim -\rho_g \nu \frac{\eta v_K}{h_d}. \quad (17)$$

This stress extracts angular momentum from the dust layer and transfers it to the gas layer. The unit surface of the dust layer loses angular momentum $\partial L_d / \partial t = r P_{\theta z}$, and the corresponding energy change is $\partial E_d / \partial t = \Omega_K \partial L_d / \partial t$. The gas layer gains the same amount of angular momentum $\partial L_g / \partial t = -r P_{\theta z}$, but the energy change is different from that of the dust layer because of the work done by the pressure gradient: $\partial E_g / \partial t = \Omega_g \partial L_g / \partial t = (1 - \eta) \Omega_K \partial L_g / \partial t$. In total, the energy liberation rate (the minus sign is added), using equations (3),(4),(6), and (17), is

$$\frac{\partial E_{\text{vis}}}{\partial t} = -(\Omega_K - \Omega_g) r P_{\theta z} = 2\eta^2 v_K^2 \Omega_K T_s \Sigma_{d,\text{vis}}, \quad (18)$$

where

$$\Sigma_{d,\text{vis}} = \frac{1}{2\sqrt{2\pi}} \frac{1 + 2T_s}{1 + T_s} \frac{1}{f_{\text{mid}}} \Sigma_d. \quad (19)$$

In the above calculation, the viscosity coefficient is modeled as $\nu = \alpha c_g h_g$. The same α is used for both D_g and ν for simplicity. The effective surface density $\Sigma_{d,\text{vis}}$ is inversely proportional to the midplane dust-to-gas ratio f_{mid} and only weakly depends on T_s . Note that the above relationship is derived for $f_{\text{mid}} \gtrsim 1$. The effective surface density for general f_{mid} is derived in Appendix C and is given by

$$\begin{aligned} \Sigma_{d,\text{vis}} &= \frac{C_{\text{str}}}{\sqrt{\pi}} f_{\text{mid}} \Sigma_d \frac{1 + 2T_s}{1 + T_s} \\ &\times \int_{-\infty}^{\infty} \frac{\beta^2 + 2\beta T_s^2 - T_s^2}{(T_s^2 + \beta^2)^2} \frac{\tilde{z}^2 \exp(-2\tilde{z}^2)}{[1 + C_{\text{str}} f_{\text{mid}} \exp(-\tilde{z}^2)]} d\tilde{z}, \end{aligned} \quad (20)$$

where

$$C_{\text{str}} = \frac{1}{T_s^2 + 1}. \quad (21)$$

Expression (20) is complicated, but for large f_{mid} , its dependence on T_s and f_{mid} is similar to that of the simpler equation (19); $\Sigma_{d,\text{vis}} \propto f_{\text{mid}}^{-0.9}$ and depends only weakly on T_s .

3.3. Energy Dissipation in Turbulence

The turbulent energy of the largest eddies transfers to smaller eddies, and finally dissipates to thermal energy via decay of the smallest eddies due to molecular viscosity. The size and velocity of the largest eddies are assumed to be $l_{g,\text{eddy}} = \alpha^{1/2} h_g$ and $u_{g,\text{eddy}} = \alpha^{1/2} c_s$. This

assumption means that the turnover time of the largest eddies is the Keplerian time ($\tau_{g,\text{eddy}} = l_{g,\text{eddy}}/u_{g,\text{eddy}} = \Omega_K^{-1}$; Cuzzi et al. 2001). Using the Kolmogorov scaling law, the energy dissipation rate per unit volume and unit time is

$$\frac{\partial \varepsilon_{\text{turb}}}{\partial t} = (\rho_g + C_{\text{ene}}\rho_d) \frac{u_{g,\text{eddy}}^2}{\tau_{g,\text{eddy}}} = (\rho_g + C_{\text{ene}}\rho_d) \alpha h_g^2 \Omega_K^3, \quad (22)$$

where the factor C_{ene} represents the fact that dust particles that are coupled only weakly to the gas do not contribute to the turbulent energy, and is given by (see Appendix D)

$$C_{\text{ene}} = \begin{cases} \frac{1}{T_s T_e + 1} & \text{for } T_s \leq T_e \\ \frac{1}{T_s^2 (T_e^{-2} + 1)} & \text{for } T_s > T_e \end{cases}, \quad (23)$$

where $T_e = \tau_{g,\text{eddy}} \Omega_K$ is the non-dimensional turnover time of the largest eddies. For most of this paper, we consider $T_e = 1$. The effect of the dust inertia is ignored for simplicity.

Energy dissipation of turbulence occurs only in the dust layer. This assumption may be problematic for $T_s \gg 1$, as discussed in §3.2, but for simplicity, we assume that energy dissipation occurs in $-\sqrt{2}h_d < z < \sqrt{2}h_d$. The dissipation rate of the energy per unit surface area and unit time is

$$\frac{\partial E_{\text{turb}}}{\partial t} = \alpha h_g^2 \Omega_K^3 \int_{-\sqrt{2}h_d}^{\sqrt{2}h_d} (\rho_g + C_{\text{ene}}\rho_d) dz = \alpha h_g^2 \Omega_K^3 \Sigma_{d,\text{turb}}, \quad (24)$$

where

$$\Sigma_{d,\text{turb}} = \Sigma_d \left[\frac{2}{\sqrt{\pi} f_{\text{mid}}} + C_{\text{ene}} \text{erf}(1) \right], \quad (25)$$

and $\text{erf}(1) = 0.8427$.

4. TURBULENCE STRENGTH

The strength of turbulence or the parameter α is determined by the balance between the energy supply rate ($\partial E_{g,\text{drag}}/\partial t$ in eq. [12] and $\partial E_{\text{vis}}/\partial t$ in eq. [18]) and the energy dissipation rate ($\partial E_{\text{turb}}/\partial t$ in eq. [24]). In steady turbulence,

$$\frac{\partial E_{\text{turb}}}{\partial t} = C_{\text{eff}} \left(\frac{\partial E_{g,\text{drag}}}{\partial t} + \frac{\partial E_{\text{vis}}}{\partial t} \right), \quad (26)$$

where the efficiency factor C_{eff} represents the fraction of the released gravitational energy that is transferred to turbulence. Comparison with the numerical simulation by JHK06 suggests that $C_{\text{eff}} = 0.19$ (see §5.2 below), and we adopt this value in this paper. From equations (8), (12), (18), and (24), the viscosity parameter is

$$\alpha = 2C_{\text{eff}} \tilde{\eta} T_s \frac{\Sigma_{d,\text{drag}} + \Sigma_{d,\text{vis}}}{\Sigma_{d,\text{turb}}}. \quad (27)$$

Note that the right-hand-side of equation (27) is a function of α through f_{mid} or β in the “surface densities” (see eqs. [14], [19], [20], [25]). Before obtaining the exact solution for α numerically, in the following two subsections, approximate solutions are derived.

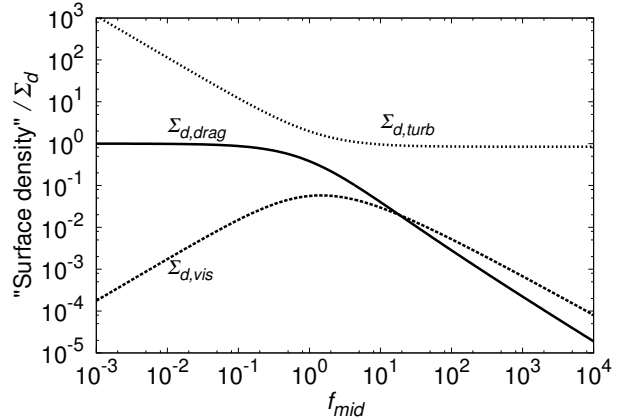


FIG. 1.— “Surface densities” $\Sigma_{d,\text{drag}}$, $\Sigma_{d,\text{vis}}$, and $\Sigma_{d,\text{turb}}$ in the small particle limit $T_s \ll 1$. The “surface densities” are normalized by the dust surface density Σ_d , and are plotted as functions of the midplane dust-to-gas ratio, f_{mid} .

4.1. Turbulence Strength in the Small-Particle Limit ($T_s \ll 1$)

In equation (27), the “surface densities”, $\Sigma_{d,\text{drag}}$, $\Sigma_{d,\text{vis}}$, and $\Sigma_{d,\text{turb}}$ represent the effective density of the dust that contributes to the liberation of the gravitational energy or dissipation in the turbulence. The “surface densities” are functions of the stopping time T_s and the midplane dust-to-gas ratio f_{mid} . For small dust particles ($T_s \ll 1$), the “surface densities” in equations (14), (20), (or approximated eqs. [13], [19]), and (25) depend on T_s only through $f_{\text{mid}} \approx Z_{\text{disk}}(T_s/\alpha)^{1/2}$. Figure 1 shows how the “surface densities” vary with f_{mid} for small particles ($T_s \ll 1$). When the midplane dust-to-gas ratio is much smaller than unity, the liberation of the gravitational energy mainly comes from the dust accreting due to individual drag, while for $f_{\text{mid}} \gg 1$, the collective drag dominates the energy liberation. For the energy dissipated in turbulence, if $f_{\text{mid}} \ll 1$, the “surface density” $\Sigma_{d,\text{turb}}$ is the column density of the gas in the dust layer and is inversely proportional to f_{mid} . If the dust layer is thin enough that $f_{\text{mid}} \gg 1$, then $\Sigma_{d,\text{turb}}$ is simply given by the dust surface density Σ_d .

Consider how the turbulent parameter α given by equation (27) depends on the stopping time T_s and the disk metallicity Z_{disk} . In the following discussion, we assume small particles, such that $T_s \ll 1$. As discussed above, for $T_s \ll 1$, the “surface densities” depend on T_s only through $f_{\text{mid}} \approx Z_{\text{disk}}(T_s/\alpha)^{1/2}$, and consequently equation (27) determines the value of α/T_s . Thus, in the limit of $T_s \ll 1$, it is seen that $\alpha \propto T_s$. We derive an approximate expression of α for the small and large limits of f_{mid} . For $f_{\text{mid}} \ll 1$, Figure 1 (and eqs. [13], [20], and [25]) show that $\Sigma_{d,\text{drag}} = \Sigma_d$, $\Sigma_{d,\text{vis}} \sim f_{\text{mid}} \Sigma_{d,\text{drag}} \ll \Sigma_{d,\text{drag}}$, and $\Sigma_{d,\text{turb}} = 2\Sigma_d/(\sqrt{\pi} f_{\text{mid}})$. Thus, the ratio of the “surface densities” in equation (27) reduces to $(\Sigma_{d,\text{drag}} + \Sigma_{d,\text{vis}})/\Sigma_{d,\text{turb}} = \sqrt{\pi} f_{\text{mid}}/2$. For $f_{\text{mid}} \gg 1$, though $\Sigma_{d,\text{drag}}$ is smaller than $\Sigma_{d,\text{vis}}$, it still makes a contribution to the energy liberation. We fit the functional form of $(\Sigma_{d,\text{drag}} + \Sigma_{d,\text{vis}})/\Sigma_{d,\text{turb}}$ for $10^2 < f_{\text{mid}} < 10^4$ by a power law form, $(\Sigma_{d,\text{drag}} + \Sigma_{d,\text{vis}})/\Sigma_{d,\text{turb}} \approx \tilde{\Sigma}_{d,0} f_{\text{mid}}^{-\delta}$, where $\delta = 0.94$, and $\tilde{\Sigma}_{d,0} = 0.71$. Using the above ex-

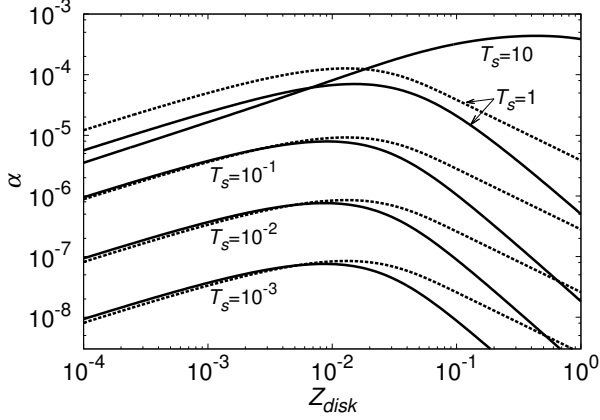


FIG. 2.— The turbulent viscosity parameter α for various values of the stopping time T_s plotted as a function of the disk metallicity Z_{disk} . The solid lines show α derived from our model. The dashed lines show α from the S98 model. We adopt an efficiency parameter of the energy supply, $C_{\text{eff}} = 0.19$, for our model, and the critical Richardson number $\text{Ri} = 0.8$ for the S98 model.

pressions, equation (27) becomes

$$\alpha = \begin{cases} (\pi^{1/2} C_{\text{eff}} \tilde{\eta} Z_{\text{disk}})^{\frac{2}{3}} T_s & \text{for } Z_{\text{disk}} \ll \sqrt{C_{\text{eff}} \tilde{\eta}} \\ (2\tilde{\Sigma}_0 C_{\text{eff}} \tilde{\eta} Z_{\text{disk}}^{-\delta})^{\frac{2}{2-\delta}} T_s & \text{for } Z_{\text{disk}} \gg \sqrt{C_{\text{eff}} \tilde{\eta}} \end{cases}, \quad (28)$$

and the midplane dust-to-gas ratio (eq.[6]) is

$$f_{\text{mid}} = \begin{cases} \left(\frac{Z_{\text{disk}}^2}{\pi^{1/2} C_{\text{eff}} \tilde{\eta}} \right)^{\frac{1}{3}} & \text{for } Z_{\text{disk}} \ll \sqrt{C_{\text{eff}} \tilde{\eta}} \\ \left(\frac{Z_{\text{disk}}^2}{2\tilde{\Sigma}_0 C_{\text{eff}} \tilde{\eta}} \right)^{\frac{1}{2-\delta}} & \text{for } Z_{\text{disk}} \gg \sqrt{C_{\text{eff}} \tilde{\eta}} \end{cases}. \quad (29)$$

The scale height of the dust layer is

$$h_d = \begin{cases} (\pi^{1/2} C_{\text{eff}} \tilde{\eta} Z_{\text{disk}})^{\frac{1}{3}} h_g & \text{for } Z_{\text{disk}} \ll \sqrt{C_{\text{eff}} \tilde{\eta}} \\ (2\tilde{\Sigma}_0 C_{\text{eff}} \tilde{\eta} Z_{\text{disk}}^{-\delta})^{\frac{1}{2-\delta}} h_g & \text{for } Z_{\text{disk}} \gg \sqrt{C_{\text{eff}} \tilde{\eta}} \end{cases}. \quad (30)$$

In the above approximate expressions (28)-(30), the upper line represents $f_{\text{mid}} \ll 1$ and the lower line represents $f_{\text{mid}} \gg 1$. The transition of these expressions occurs at $f_{\text{mid}} \sim 1$, which corresponds to $Z_{\text{disk}} \sim \sqrt{C_{\text{eff}} \tilde{\eta}}$, and a maximum value of α ,

$$\alpha_{\text{max}} \sim C_{\text{eff}} \tilde{\eta} T_s. \quad (31)$$

4.2. Turbulence Strength for a Small Dust-to-Gas Ratio ($f_{\text{mid}} \ll 1$)

We derive the approximate expression of the turbulent strength α as a function of T_s and Z_{disk} in the limit of small dust-to-gas ratio at the midplane, $f_{\text{mid}} \ll 1$, but without assuming $T_s \ll 1$. For $f_{\text{mid}} \ll 1$, the ‘‘surface densities’’ (eqs. [14], [20], and [25]) reduce to $\Sigma_{d,\text{drag}} = \frac{1}{2} \Sigma_d (T_s^2 + 2) / (T_s^2 + 1)^2$, $\Sigma_{d,\text{vis}} \sim f_{\text{mid}} \Sigma_{d,\text{drag}} \ll \Sigma_{d,\text{drag}}$, and $\Sigma_{d,\text{turb}} = 2 \Sigma_d / (\sqrt{\pi} f_{\text{mid}})$. Thus, the approximate expression of equation (27) becomes

$$\alpha = \left[\frac{\sqrt{\pi}}{2} C_{\text{eff}} \tilde{\eta} Z_{\text{disk}} \sqrt{\frac{1+2T_s}{1+T_s} \frac{T_s^2+2}{(T_s^2+1)^2}} \right]^{\frac{2}{3}} T_s. \quad (32)$$

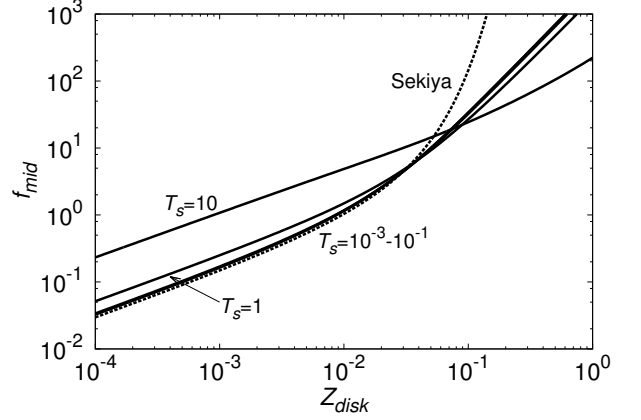


FIG. 3.— The midplane dust-to-gas ratio f_{mid} . The solid lines are calculated for various values of the stopping time T_s using our model. The dashed line is taken from the S98 model. The midplane dust-to-gas ratio and the scale height of the dust layer are, respectively,

$$f_{\text{mid}} = \left[\frac{2Z_{\text{disk}}^2}{\sqrt{\pi} C_{\text{eff}} \tilde{\eta}} \frac{1+2T_s}{1+T_s} \frac{(T_s^2+1)^2}{T_s^2+2} \right]^{\frac{1}{3}}, \quad (33)$$

and

$$h_d = \left[\frac{\sqrt{\pi}}{2} C_{\text{eff}} \tilde{\eta} Z_{\text{disk}} \frac{1+T_s}{1+2T_s} \frac{T_s^2+2}{(T_s^2+1)^2} \right]^{\frac{1}{3}} h_g. \quad (34)$$

4.3. Turbulence Strength and Dust Layer Thickness

The properties of the turbulent viscosity parameter α for $T_s \ll 1$ or $f_{\text{mid}} \ll 1$ are described in the last two subsections. For general T_s and f_{mid} , equation (27) must be solved numerically. We use the van Wijngaarden-Dekker-Brent method (Press et al. 1986) to obtain α from equation (27). In Figure 2, the solid lines represent the variation of α with the disk metallicity Z_{disk} for various values of the particle stopping time T_s . It is seen that, for small dust particles ($T_s \lesssim 1$), α is proportional to T_s , as discussed in §4.1. The maximum $\alpha_{\text{max}} \sim C_{\text{eff}} \tilde{\eta} T_s$ appears at $Z_{\text{disk}} \sim \sqrt{C_{\text{eff}} \tilde{\eta}} \sim 10^{-2}$ (and $f_{\text{mid}} \sim 1$) for $T_s \lesssim 1$. The turbulence weakens as Z_{disk} deviates from $\sqrt{C_{\text{eff}} \tilde{\eta}}$ ($\alpha \propto Z_{\text{disk}}^{2/3}$ for $Z_{\text{disk}} \lesssim \sqrt{C_{\text{eff}} \tilde{\eta}}$, and $\alpha \propto Z_{\text{disk}}^{-1.8}$ for $Z_{\text{disk}} \gtrsim \sqrt{C_{\text{eff}} \tilde{\eta}}$, see eq. [28]). For particles of $T_s > 1$, α peaks at a larger Z_{disk} (or f_{mid}).

Figure 3 shows the variation in the midplane dust-to-gas ratio f_{mid} with the disk metallicity Z_{disk} . For small particles ($T_s \lesssim 1$), α is proportional to T_s , and the midplane dust-to-gas ratio $f_{\text{mid}} \propto (T_s/\alpha)^{1/2}$ does not depend on T_s . For a small dust-to-gas ratio ($f_{\text{mid}} \ll 1$), $f_{\text{mid}} \propto Z_{\text{disk}}^{2/3}$, and for $f_{\text{mid}} \gg 1$, $f_{\text{mid}} \propto Z_{\text{disk}}^{1.9}$. Note that if the disk metallicity is larger than 0.2, then the midplane dust-to-gas ratio becomes as large as 100, which is high enough to induce a gravitational instability in the dust layer. This result is consistent with the previous works by, e.g., S98. Figure 4 shows that the dust layer thickness h_d is of the order of $10^{-3} - 10^{-2}$ times the thickness of the gas disk.

5. COMPARISONS WITH PREVIOUS STUDIES

In this section, the dust layer model that is based on the energetics of dust accretion is compared with results

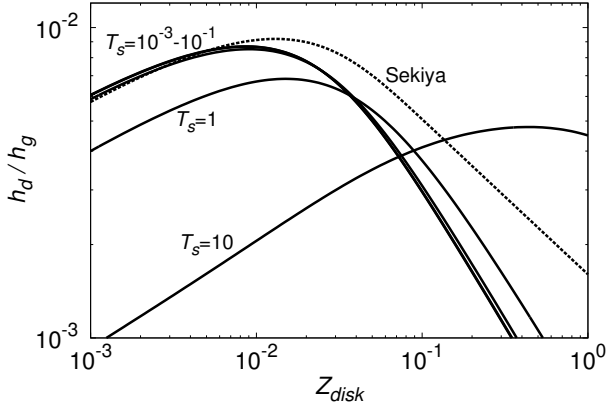


FIG. 4.— The scale height of the dust layer h_d normalized by the gas scale height h_g . The solid lines are calculated for various values of the stopping time T_s by our model. The dashed line is taken from the S98 model, which is calculated using equation (38).

from previous work. Previous studies have analyzed the detailed physics of the dust layer, including the onset of KH or streaming instabilities, and several stabilizing effects, such as Keplerian shear, using both analytical and numerical approaches. It is of interest to determine which properties of the dust layer are reproduced by our model and which are missing.

5.1. Comparison with Previous Analytical Studies

5.1.1. Comparison with Sekiya (1998)

S98 analytically solved the density structure of the dust layer, assuming that the layer structure was adjusted to be marginally unstable to KH instability. To obtain the density structure, S98 assumed that the Richardson number remained close to the critical value for instability throughout the dust layer. S98 considered small dust particles that were tightly coupled to the gas ($T_s \ll 1$), and treated the gas and the dust as a single fluid. Then, the density structure of the dust layer was calculated for various values of the disk metallicity Z_{disk} . In S98, the dust layer structure was determined by the argument for the stability of a stratified fluid, not by the balance between sedimentation and diffusion of the dust. However, it is possible to interpret the result of S98 as follows: The turbulent strength in the dust layer is adjusted such that the turbulent diffusion of the dust maintains the marginally unstable density structure. Using this interpretation, we calculate the effective value of the turbulent diffusion parameter α as a function of Z_{disk} for $T_s \ll 1$.

From equation (22) of S98, the midplane dust-to-gas ratio, f_{mid} , is related to the disk metallicity, Z_{disk} , as

$$Z_{\text{disk}} = \sqrt{\frac{2\text{Ri}\tilde{\eta}}{\pi}} \left\{ \ln \left[\left(1 + \sqrt{1 - \left(\frac{1}{1+f_{\text{mid}}} \right)^2} \right) (1+f_{\text{mid}}) \right] - \sqrt{1 - \left(\frac{1}{1+f_{\text{mid}}} \right)^2} \right\}, \quad (35)$$

where the Richardson number Ri is constant throughout the dust layer, and the self-gravity of the dust layer is

neglected. The dust density distribution is given by

$$\frac{\rho_d}{\rho_g} = \left[\frac{z^2}{\text{Ri}\tilde{\eta}h_g^2} + \left(\frac{1}{1+f_{\text{mid}}} \right)^2 \right]^{-\frac{1}{2}} - 1. \quad (36)$$

The half-thickness of the dust layer, z_d , at which the dust density becomes zero, is given by

$$z_d = \sqrt{\text{Ri}\tilde{\eta} \left[1 - (1+f_{\text{mid}})^{-2} \right]} h_g. \quad (37)$$

To compare with the scale height of Gaussian distribution, h_d , we define the scale height of the dust distribution as the vertical dispersion of the dust particles,

$$h_{d,\text{Sek}}^2 = \frac{\int_0^{z_d} z^2 \rho_d dz}{\int_0^{z_d} \rho_d dz}. \quad (38)$$

The turbulent parameter α_{Sek} is estimated from equation (4), using $T_s \ll 1$, as

$$\alpha_{\text{Sek}} = \left(\frac{h_{d,\text{Sek}}}{h_g} \right)^2 T_s. \quad (39)$$

For $f_{\text{mid}} \gtrsim 1$, equation (37) reduces to $z_d \approx (\text{Ri}\tilde{\eta})^{1/2} h_g$. Substituting this expression into $h_{d,\text{Sek}} \approx z_d$ of equation (39) gives

$$\alpha_{\text{Sek}} \approx \text{Ri}\tilde{\eta} T_s \quad \text{for } f_{\text{mid}} \gtrsim 1, \quad (40)$$

which can be compared with equation (31). For $f_{\text{mid}} \ll 1$, equation (35) is approximated in the lowest order of f_{mid} as

$$Z_{\text{disk}} = \frac{4}{3} \sqrt{\frac{\text{Ri}\tilde{\eta}}{\pi}} \left[f_{\text{mid}}^{3/2} + O(f_{\text{mid}}^{5/2}) \right]. \quad (41)$$

Thus, the midplane dust-to-gas ratio is

$$f_{\text{mid}} = \left(\frac{9}{16} \frac{\pi}{\text{Ri}\tilde{\eta}} Z_{\text{disk}}^2 \right)^{\frac{1}{3}}. \quad (42)$$

For $f_{\text{mid}} \ll 1$ and $z \ll h_g$, the dust density distribution (eq.[36]) is

$$\frac{\rho_d}{\rho_g} \approx f_{\text{mid}} \left[1 - \frac{1}{2\text{Ri}\tilde{\eta}f_{\text{mid}}} \left(\frac{z}{h_g} \right)^2 \right]. \quad (43)$$

To the order of $(z/h_d)^2$, this distribution is approximated by the Gaussian distribution $f_{\text{mid}} \exp[-z^2/(2h_{d,\text{Sek}}^2)] \approx f_{\text{mid}}[1 - z^2/(2h_{d,\text{Sek}}^2)]$, and its scale height $h_{d,\text{Sek}}$ is

$$h_{d,\text{Sek}} \approx \sqrt{\text{Ri}\tilde{\eta}f_{\text{mid}}} h_g \approx \left[\frac{3\text{Ri}}{4} \pi^{1/2} Z_{\text{disk}} \tilde{\eta} \right]^{\frac{1}{3}} h_g. \quad (44)$$

The turbulent parameter α_{Sek} of equation (39) is

$$\alpha_{\text{Sek}} \approx \left[\frac{3\text{Ri}}{4} \pi^{1/2} Z_{\text{disk}} \tilde{\eta} \right]^{\frac{2}{3}} T_s \quad \text{for } f_{\text{mid}} \ll 1. \quad (45)$$

Comparing this expression to equation (28) provides a relationship between the energy supply efficiency to turbulence, C_{eff} , and the critical Richardson number, Ri , as $C_{\text{eff}} = (3/4)\text{Ri}$. In the above discussion on α_{Sek} , we used

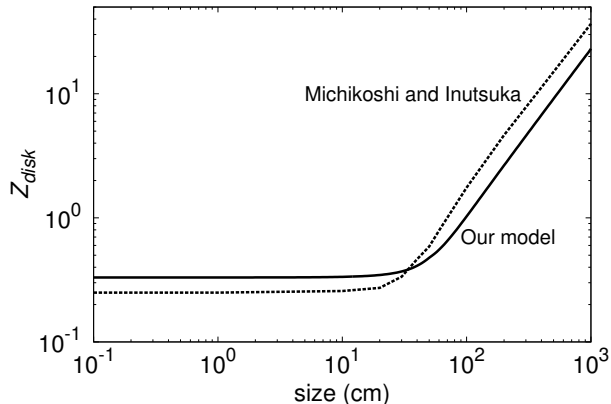


FIG. 5.— Comparison with the results in Michikoshi & Inutsuka (2006). The solid line shows the relationship between the midplane dust-to-gas ratio f_{mid} and the particle radius a . The dashed line shows the boundary at which the growth rate of the KH instability is $\omega = 0.1$ (above the dashed line, $\omega > 0.1$). We use the same disk model that is adopted in Michikoshi & Inutsuka (2006). The dashed line is read from Fig. 16 in Michikoshi & Inutsuka (2006).

the dust layer thickness $h_{d,\text{Sek}}$ derived from the Gaussian fit. However, the thickness defined by the vertical dispersion (eq.[38]) in the small f_{mid} limit is 0.63 times thinner than that defined by the Gaussian fit. Thus, the energy supply efficiency is $0.4 = 0.63^2$ times smaller than the above estimate and thus $C_{\text{eff}} \approx 0.3\text{Ri}$. The relationship between C_{eff} and Ri can also be derived by comparing the expressions for f_{mid} (eqs. [29] and [42]) as $C_{\text{eff}} = 16/(9\pi^{3/2})\text{Ri} \approx 0.3\text{Ri}$. We compare our result with the numerical simulation developed by JHK06, which will be discussed in §5.2. The comparison with this simulation suggests a slightly smaller energy supply efficiency,

$$C_{\text{eff}} \approx 0.24\text{Ri}. \quad (46)$$

The turbulent parameter α_{Sek} given by equation (39) is numerically calculated and is plotted using dashed lines in Figure 2. The critical Richardson number $\text{Ri} = 0.8$ is adopted to fit the simulation results provided by JHK06. For $Z_{\text{disk}} \ll 1$ and $T_s \lesssim 1$, the solid and dashed lines agree with each other very well. This is expected from the above discussion that the dependence of α and α_{Sek} on Z_{disk} and T_s for small f_{mid} are the same (eqs. [28] and [45]). For $Z_{\text{disk}} \gtrsim 10^{-2}$, a deviation between the solid and dashed lines appears, and the difference increases with Z_{disk} . We note that for $Z_{\text{disk}} \gtrsim 0.1$, the S98 density distribution shows a cusp at the midplane, which is a significant difference from the Gaussian distribution of our model. In Figure 3, the midplane dust-to-gas ratio of the S98 model is plotted with a dashed line. For small $Z_{\text{disk}} \lesssim 0.05$, the result from S98 is consistent with our result (the dashed line coincides with the solid lines for $T_s \lesssim 1$). For $Z_{\text{disk}} \gtrsim 0.05$, the midplane dust-to-gas ratio from the S98 model is larger than our results. Both results are still qualitatively consistent, indicating that, for $Z_{\text{disk}} \gtrsim 0.1$, the midplane dust-to-gas ratio becomes large enough for gravitational instability ($f_{\text{mid}} \sim 100$).

5.1.2. Comparison with Michikoshi & Inutsuka (2006)

Michikoshi & Inutsuka (2006) analyzed the growth rate of the KH instability of a dust layer, taking into account the relative motion and the friction between the dust and

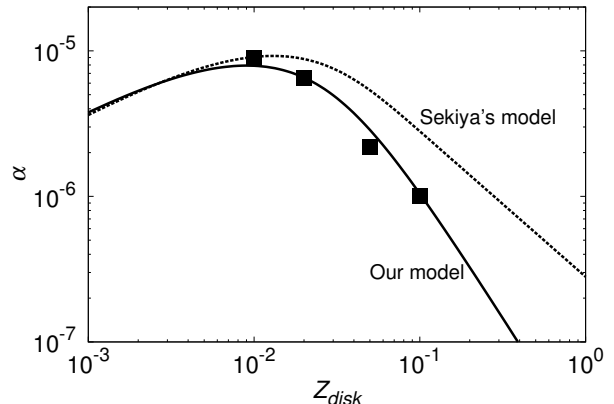


FIG. 6.— The turbulent viscosity parameter α estimated from our model, compared with the simulation described in JHK06. The solid line is calculated from our model and the dashed line is taken from the S98 model. The squares are the simulation results, δ_i in Table 2 of JHK06. The stopping time $T_s = 0.1$ is adopted both for our model and the simulation.

the gas. Their formulation does not assume tight dust-gas coupling, and thus it can be applied to scenarios involving large dust particles ($T_s \gg 1$), while the vertical gravity, Coriolis force, and Keplerian shear are neglected. The initial velocity gradient in the vertical direction is caused by the dust inertia, using the formula provided in NSH86. The growth rate of instability has been derived for a wide range of dust sizes a and midplane dust-to-gas ratios f_{mid} , and is summarized in their Figure 16. They argued that if the effect of Keplerian shear is taken into account, the line corresponding to the growth rate $\omega = 1$ in the a - f_{mid} plane would be the boundary between the stable and unstable configurations. This marginally unstable structure of the dust layer presented by Michikoshi & Inutsuka (2006) can be considered an extension of the S98 model for general sizes of the dust particles, and provides a reference to be compared with our model.

In Figure 5, we compare our model in the a - f_{mid} plane with the line at which the growth rate ω has a constant critical value. We adopt the critical growth rate as $\omega = 0.1$, which is smaller than the value Michikoshi & Inutsuka (2006) suggested. The qualitative behavior does not differ between $\omega = 0.1$ and $\omega = 1$. Our model well reproduces the result of Michikoshi & Inutsuka (2006). The agreement of our model with the results of S98 and of Michikoshi & Inutsuka (2006) suggests that the onset of KH instability is controlled by the energy supply due to dust accretion over a wide range of particle sizes, a , or stopping times, T_s . It must be noted, however, that the initial state assumed in Michikoshi & Inutsuka (2006) is such that the vertical velocity shear appears only in the dust layer, neglecting the velocity shear in the Ekman-like boundary layer that may appear between the dust layer and the upper gas layer. This is the same assumption that we adopt. As discussed in §3.2, this assumption is appropriate for small dust particles ($T_s \lesssim 1$), while for large particles ($T_s \gg 1$) the vertical velocity profile of the thick turbulent boundary layer may quickly deviate from that given by NSH86. Though the agreement with the result by Michikoshi & Inutsuka (2006) shows the applicability of our model to KH instability in the dust layer for general values of T_s , we should keep in mind the limitation of the models mentioned above.

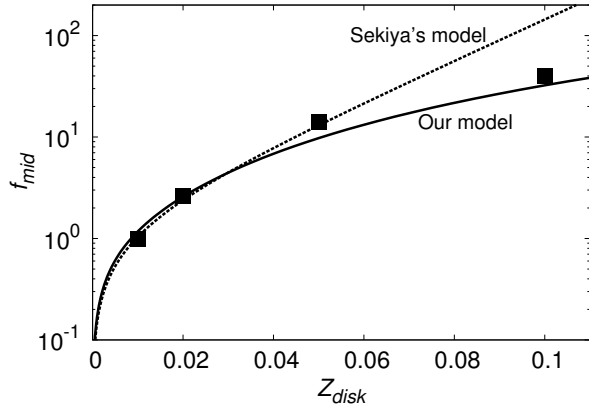


FIG. 7.— Midplane dust-to-gas ratio f_{mid} derived from analytical models and from the simulation described in JHK06. The solid line is calculated from our model and the dashed line is taken from the S98 model. The squares are the simulation results, which are read from Figure 13 of JHK06. The stopping time is $T_s = 0.1$.

5.2. Comparison with Previous Numerical Simulations

5.2.1. Comparison with Johansen et al. (2006)

Numerical simulations of KH instability induced by formation of a dust layer were presented in JHK06. Their two-dimensional simulation on the θz -plane solved for both the gas and dust motions. They obtained a quasi-steady or oscillating density distribution of the dust in which dust settling and turbulent diffusion balanced each other. The diffusion coefficient in the vertical direction, δ_t , was measured from the scale height of the dust layer and was summarized in their Table 2. In Figure 6, the turbulent viscosity parameter α of equation (27) (the solid line) is compared with the diffusion coefficient measured from the simulation (the squares). To fit the simulation result, the efficiency parameter of the energy supply to turbulence, C_{eff} , is set to 0.19. We also fit the turbulent diffusion parameter for the density distribution of S98, α_{Sek} , to the simulation. We adopt the critical Richardson number as $\text{Ri} = 0.8$ for fitting. This is slightly smaller than the value JHK06 suggested ($\text{Ri} = 1.0$). It is seen that the numerical simulation is well explained both by our model and the S98 model. This means that the dust layer is maintained so as to provide a constant Richardson number, and in the parameter range that JHK06 surveyed ($0.01 < Z_{\text{disk}} < 0.1$), this critical Richardson number does not vary significantly with the disk metallicity Z_{disk} . (The recent result by Lee et al. (2010), in which they argue that Ri is proportional to Z_{disk} if the Keplerian shear is taken into account, will be discussed later in this subsection.) Because the efficiency parameter C_{eff} in our model is proportional to the critical Richardson number, as shown in equation (46), the efficiency parameter C_{eff} is also expected to be constant for $0.01 < Z_{\text{disk}} < 0.1$.

A comparison of the midplane dust-to-gas ratio between our model and the simulation is shown in Figure 7. The simulation is well fitted by our model (the solid line) and also by the S98 model (the dashed line). For $Z_{\text{disk}} = 0.1$, the S98 model predicts larger f_{mid} than the simulation. This may be because the simulation does not have enough resolution to resolve the density structure around the midplane at which the S98 model expects a rapid increase in the dust density. If this is the case,

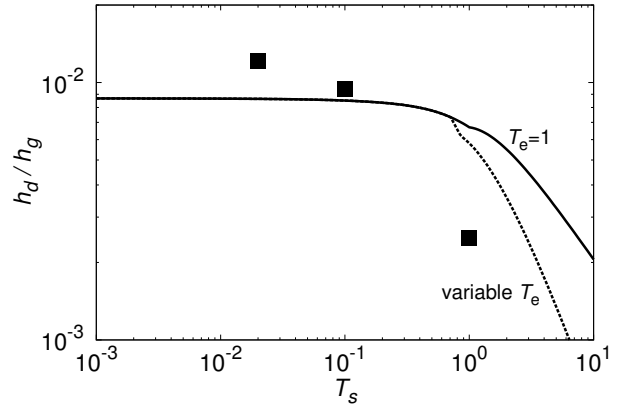


FIG. 8.— The scale heights of the dust layer h_d estimated from our model and from the JHK06 simulation are plotted versus the stopping time T_s . The solid line is calculated assuming that the turnover time of the largest eddies is the Keplerian ($T_e = 1$). The dashed line includes the variable T_e calculated by equation (48). The squares are the simulation results, $\langle z^2 \rangle^{1/2} / H$ in Table 2 of JHK06. The disk metallicity is $Z_{\text{disk}} = 10^{-2}$.

it is difficult to judge whether our model or the model presented by S98 is the best fit with the simulation.

Figure 8 shows the variation in dust layer thickness with T_s from our model and compares this variation with the simulation results. In plotting Figure 6 in the last paragraph, the turbulent viscosity parameter α was calculated from equation (4) using the dust layer thickness h_d measured from the simulation. However, it is not clear if equation (4) is still valid for large T_s because this equation assumes that the turnover time of the largest eddies is equal to the Keplerian time (YL07), and as discussed below this assumption may not be appropriate for large T_s . Thus, in Figure 8, the dust layer thickness is plotted directly without transferring to α . In our model, the dust layer thickness h_d is constant for $T_s \lesssim 1$ and decreases slowly with T_s for $T_s \gtrsim 1$ (the solid line), although in the simulation it decreases more rapidly with T_s . The discrepancy between our model and the simulation is apparent for $T_s = 1$. The difference is as large as a factor of 3, but it causes an order of magnitude discrepancy in $\alpha \propto h_d^2$. This discrepancy suggests that our model predicts turbulent diffusion that is too large for $T_s \gtrsim 1$. In fact, for large T_s in our model, the dust layer thickness becomes smaller than the size of the largest eddies, contradicting our assumption that the turbulent layer coincides with the dust layer (see, however, the discussion in §3.2 on the validity of this assumption, and see also eq. [56] of YL07 for a possible physical reason for $l_{g,\text{eddy}} > h_d$). From equation (4) and $l_{g,\text{eddy}} = \alpha^{1/2} h_g$, the condition for the dust layer thickness to be larger than the largest eddy size ($h_d > l_{g,\text{eddy}}$) is $T_s < 1/\sqrt{2}$. Thus, for $T_s > 1/\sqrt{2}$, our model results in a dust layer that is too thick (or an eddy size that is too small). One possible remedy for this situation is to remove the assumption that the turnover time of the largest eddies is equal to the Keplerian time. By introducing a parameter ξ ($0 \leq \xi \leq 1/2$), the largest eddy size and the velocity are expressed as $l_{g,\text{eddy}} = \alpha^{(1/2)+\xi} h_g$ and $u_{g,\text{eddy}} = \alpha^{(1/2)-\xi} c_s$. The non-dimensional turnover time of the largest eddies is $T_e = (l_{g,\text{eddy}}/u_{g,\text{eddy}})\Omega_K = \alpha^{2\xi}$. The dust layer thickness for $T_e \neq 1$ is provided by equa-

tion (21) of YL07,

$$h_d = \sqrt{\frac{\alpha}{T_s}} \left(1 + \frac{T_s T_e^2}{T_s + T_e}\right)^{-1/2} h_g. \quad (47)$$

For $T_s > 1/2$, we impose the condition that the largest eddy size $l_{g,\text{eddy}} = \alpha^{(1/2)+\xi} h_g$ is equal to the above h_d . This condition determines the turnover time by the equation

$$T_s T_e (T_s + T_e + T_s T_e^2) - T_s - T_e = 0. \quad (48)$$

Using this T_e (or ξ), the turbulent viscosity parameter α and the dust layer thickness h_d are recalculated and plotted with the dashed line in Figure 8. As expected, the introduction of a new parameter T_e suppresses the largest eddy size and the turbulent diffusion of dust particles for $T_s > 1/\sqrt{2}$, improving the comparison with the simulation result. However, we need to determine whether the turnover time of the largest eddies, $T_e \Omega_K^{-1} = \alpha^{2\xi} \Omega_K^{-1}$, in the simulation presented in JHK06 for $T_s = 1$ is actually smaller than the Keplerian time, as equation (48) predicts. Cuzzi et al. (1993) argue that, based on laboratory measurements, the eddy turnover time in an Ekman layer would be smaller than the Keplerian time by a factor 20 – 80. The turbulent layer possibly behaves as an Ekman layer for $T_s > 1$, as discussed in §3.2. We are currently performing numerical simulations using the same conditions as JHK06 to investigate the turbulence for $T_s \gtrsim 1$ in more detail (Ishitsu et al., in preparation).

Lee et al. (2010) performed a three-dimensional numerical simulation of the onset of KH instability. They solved simplified equations in which the dust and the gas were treated as a single fluid, but they included the effect of the Keplerian shear in the radial direction. They found that the radial shear stabilizes the KH instability, and the critical Richardson number for instability is not always the standard value, 0.25, but can be much smaller if the stabilizing effect of the radial shear is significant (see also Ishitsu & Sekiya 2003). Equation (32) in Lee et al. (2010) shows that the ratio of the stabilizing effect by the radial shear to the destabilizing effect by the vertical shear is proportional to $\text{Ri}(1 + f_{\text{mid}})/f_{\text{mid}} \approx \text{Ri}/f_{\text{mid}}$ for $f_{\text{mid}} \ll 1$, and thus the critical Richardson number should scale as $\text{Ri} \propto f_{\text{mid}}$. In our model, we assume that the energy supply efficiency C_{eff} , which is proportional to the critical Richardson number (eq.[46]), is constant. However, the simulation in Lee et al. (2010) suggests that C_{eff} should also be proportional to f_{mid} (even for $f_{\text{mid}} \gtrsim 1$). If this is the case, dependence of f_{mid} on Z_{disk} would be milder than that shown in Figure 3 ($f_{\text{mid}} \propto Z_{\text{disk}}^{1/2}$ for $f_{\text{mid}} \ll 1$ and $f_{\text{mid}} \propto Z_{\text{disk}}^{0.97}$ for $f_{\text{mid}} \gg 1$). The effect of the radial shear was not included in the simulation presented in JHK06, with which we compared our model in detail, because their simulation was two-dimensional in the θz -plane. Extending JHK06 to three dimensions and including the radial shear effect are crucial to determining how the energy supply efficiency C_{eff} behaves as f_{mid} varies.

5.2.2. Comparison with Bai & Stone (2010)

Bai & Stone (2010) performed a three-dimensional simulation, focusing on investigating turbulence induced by streaming instability. They found that the streaming instability induced turbulence before the KH instability set

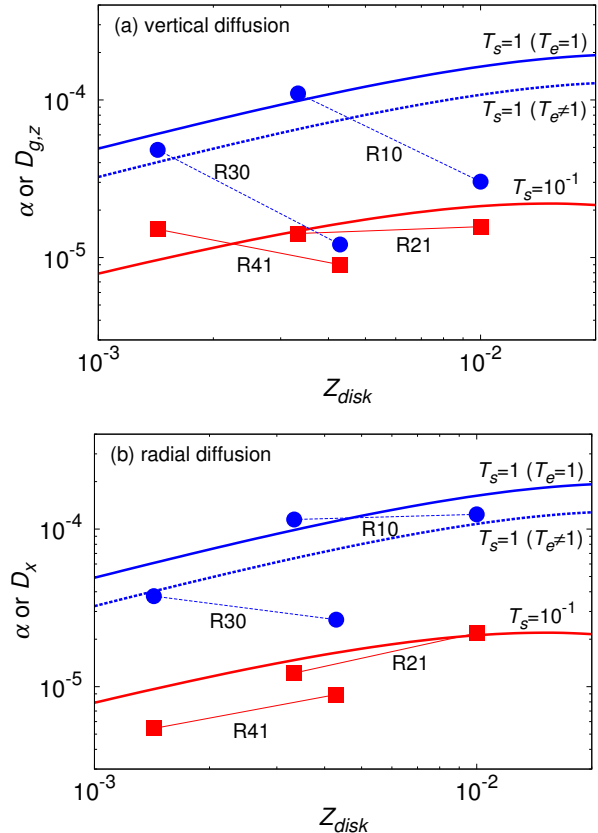


FIG. 9.— The turbulent viscosity parameter α estimated from our model for $T_s = 10^{-1}$ and 1 is compared with the simulation presented in Bai & Stone (2010). The solid line is calculated assuming the turnover time of the largest eddies is the Keplerian time ($T_e = 1$). The dashed line includes the variable T_e calculated from equation (48). (a) Comparison with the vertical diffusion coefficient, $D_{g,z}$ (3D), measured in the simulation (Table 2 of Bai & Stone 2010). The squares and circles are the simulation results, connected by lines that indicate which runs have the same size distribution of dust particles. The label of run Rxy means the particle size distribution is such that the stopping time ranges $T_s \in [10^{-x}, 10^{-y}]$, e.g., in run R30, $T_s \in [10^{-3}, 10^0]$. In each run, the disk metallicity Z is 0.01 and 0.03. To compare the results with our model, we assume that only the largest particles contribute to turbulence, and that the effective metallicity is estimated by $Z_{\text{disk}} = Z/N_{\text{type}}$, where $N_{\text{type}} = 3$ (R10 and R21) or 7 (R30 and R41) is the number of particle species. We compare our model of $T_s = 1$ with runs R10 and R30 (plotted in blue), and the model of $T_s = 10^{-1}$ with runs R41 and R21 (plotted in red). (b) Comparison with the radial diffusion coefficient, D_x , measured in the 3D runs of the simulation. We assume that the diffusion coefficient of the gas is represented by that of the smallest particles in the simulation. The values of D_x for the smallest particles are read from Fig.9 of Bai & Stone (2010).

in. They measured the turbulent diffusion coefficient. However, it is difficult to compare our model directly with the results in Bai & Stone (2010), because their simulation includes particles of several sizes (3-7 species) while our model considers only single-sized particles. In the simulation, it was reported that only large particles were responsible for inducing turbulence. Our model also shows that the energy liberation per unit mass of the dust is higher for larger particles (it is proportional to T_s for $T_s \lesssim 1$). In order to compare results, we assume that in the simulation, the turbulence is induced only by the largest particles (i.e., particles of largest T_s). For example, in the R41 run (in which the stopping time of

the particles ranges from 10^{-4} to 10^{-1}), we assume that only $T_s = 0.1$ particles are responsible for turbulence. We then compare the simulation result with our model of $T_s = 0.1$. In the simulation, each species has the same amount of mass. Because we consider the largest particles only, the total amount of the dust participating in driving turbulence is Σ_d/N_{type} , where N_{type} is the number of particle species in the simulation. For example, in the R41 run, $N_{\text{type}} = 7$, and we compare the simulation with a disk metallicity $Z = 0.01$ with our model of $Z_{\text{disk}} = Z/N_{\text{type}} = 1.43 \times 10^{-3}$.

Figure 9a shows a comparison of the diffusion coefficient obtained from the simulation ($D_{g,z}(3D)$ in Table 2 of Bai & Stone (2010)) with our model (calculated with the parameter $\tilde{\eta} = 0.05^2$, which was adopted by Bai & Stone (2010)). Although our model of $T_s = 0.1$ agrees with simulations R41 and R21 (plotted in red), we note a qualitative discrepancy between the $T_s = 1$ model and simulations R30 and R10 (plotted in blue). The simulations indicate that the diffusion coefficient decreases with the disk metallicity, and that its value for $Z = 0.03$ is about an order of magnitude smaller than the value from our model. This discrepancy cannot be resolved, even by varying the turnover time of the largest eddies T_e (the dashed line). One possible cause for the inconsistency is particle clumping and concentration in turbulent eddies, which are not included in our model. The simulation shows strong particle clumping when $Z = 0.03$ in the R10 run and also temporal clumping for $Z = 0.03$ in the R30 run. Such clumping of particles in turbulent eddies may suppress diffusion of particles compared to the no-clumping cases of $Z = 0.01$ and could be a cause of a decrease in α when Z is increased in the simulation. Even if the largest particles (of $T_s \sim 1$) concentrate in clumps, the smallest particles (of $T_s \lesssim 0.1$) do not clump, and continue to follow the turbulent diffusion of the gas (Fig. 7 of Bai & Stone 2010). In Figure 9b, the turbulent diffusion coefficient in the “radial direction” of the smallest particles in the simulation, D_x , is compared with the “vertical” diffusion coefficient α in our model. Note that we compare diffusion coefficients in the different directions. Since the smallest particles spread out to high altitudes where turbulence is weak, it is difficult to measure the vertical diffusion coefficient for the smallest particles in the simulation. In Figure 9b, though we still see a discrepancy compared with the R30 run, our model appears more consistent with the simulation results, suggesting that our model properly predicts the “gas” diffusion coefficient.

6. DISCUSSION

6.1. The Radial Drift Velocity and Collision Velocity of Dust Particles

If the dust-to-gas ratio in the dust layer were larger than unity, the radial drift velocity of dust particles would be lower than the value that the particles would have in a gas-rich environment because the gas drag force could not accelerate sufficiently against the large inertia of the dust. This effect was pointed out by NSH86 and is seen in equation (A14) for the radial velocity due to individual drag. If the dust-to-gas ratio were much larger than unity, dust accretion would be caused by collective drag exerted from the slower-orbiting upper gas

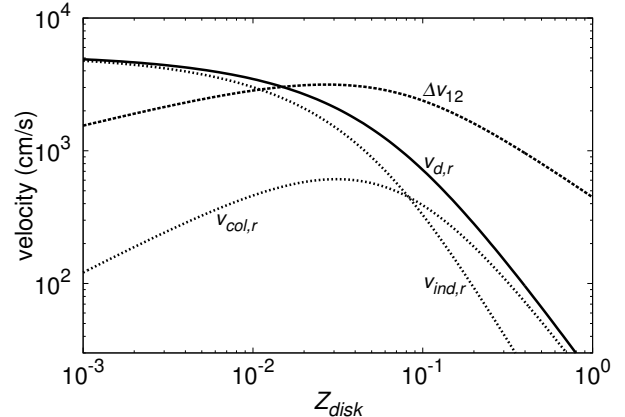


FIG. 10.— The radial drift velocity, $\bar{v}_{d,r}$ (solid line), and the relative velocity of particles due to turbulence, Δv_{12} (dashed line). The contributions of individual drag, $\bar{v}_{\text{ind},r}$, and collective drag, $\bar{v}_{\text{col},r}$, to the radial drift velocity are plotted with dotted lines.

layer (Weidenschilling 2003). The radial drift velocity of the dust is thus a function of the turbulence strength, α . For weaker turbulence, the dust-to-gas ratio in the dust layer is higher, and the individual drag is weaker. The collective drag is also weaker at smaller α because the Reynolds stress $P_{\theta z}$ is proportional to α . The relative velocity (or collision velocity) of the dust particles is also a function of α . The radial drift and collision velocities are the important factors in the dust growth process. In the previous sections, the turbulence strength α and the dust layer thickness h_d have been determined self-consistently. Using these results, the radial drift velocity and collision velocity of the dust particles are estimated.

The radial drift velocity is calculated separately for the components due to individual drag and due to collective drag. For each component, the radial drift velocity is averaged in the vertical direction. First, the averaged value of the radial drift velocity due to individual drag is calculated from equation (A14),

$$\begin{aligned} \bar{v}_{\text{ind},r} &= \frac{1}{\Sigma_d} \int_{-\infty}^{\infty} \rho_d v_{d,r} dz \\ &= -2\eta v_K T_s \frac{1}{\Sigma_d} \int_{-\infty}^{\infty} \rho_d \frac{1}{T_s^2 + \beta^2} dz. \end{aligned} \quad (49)$$

The radial drift velocity due to collective drag is calculated from the vertically-averaged angular momentum loss of the dust component. Integrating equation (C4) gives,

$$\frac{dL_d}{dt} = \int_{-\infty}^{\infty} \frac{\partial l_d}{\partial t} dz = -2\eta v_K^2 T_s \Sigma_{d,\text{vis}}, \quad (50)$$

where $\Sigma_{d,\text{vis}}$ is given by equation (C10). This angular momentum loss causes a radial drift velocity $\bar{v}_{\text{col},r}$ given by

$$\bar{v}_{\text{col},r} = \frac{2}{v_K \Sigma_d} \frac{dL_d}{dt} = -4\eta v_K T_s \frac{\Sigma_{d,\text{vis}}}{\Sigma_d}. \quad (51)$$

The total radial drift velocity is $\bar{v}_{d,r} = \bar{v}_{\text{ind},r} + \bar{v}_{\text{col},r}$, and is shown in Figure 10 as a solid line, for the case in which the particle size is chosen to maximize the radial velocity ($T_s = 1$). In plotting this figure, we adopt the model parameters at 1 AU of the minimum-mass-solar-nebula model of Hayashi (1981): $h_g/r = 0.0326$, $\eta = 1.80 \times 10^{-3}$,

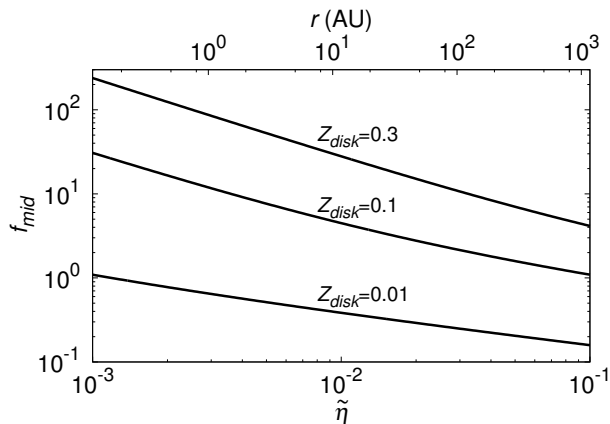


FIG. 11.— The midplane dust-to-gas ratio f_{mid} is plotted against $\tilde{\eta}$ for various values of the disk metallicity Z_{disk} . The top axis shows the corresponding radii in the gas disk model by Hayashi (1981), in which the disk temperature is $T = 278(r/\text{AU})^{-1/2}\text{K}$. The dust particles are assumed to be small ($T_s \ll 1$) such that f_{mid} is independent of T_s .

and $\tilde{\eta} = 2.92 \times 10^{-3}$. For a small disk metallicity Z_{disk} , the radial drift velocity is as large as 50 m s^{-1} , and it decreases with Z_{disk} . For $Z_{\text{disk}} > 0.08$, the radial velocity is dominated by collective drag (see the dotted lines) as pointed out by Weidenschilling (2003). For such large Z_{disk} , the radial drift velocity due to collective drag also decreases with Z_{disk} , and then it becomes as small as 1 m s^{-1} for $Z_{\text{disk}} = 0.2$. The radial drift velocity is strongly suppressed for a sufficiently massive dust layer.

The relative velocity of dust particles due to turbulence, Δv_{12} , is calculated for $T_s = 1$ by substituting $\text{St}_1 = 1$ and $\text{St}_2 = 0$ into equation (29) in Ormel & Cuzzi (2007), and is shown in Figure 10 as a dashed line. The collision velocity is estimated by the larger of Δv_{12} and $\bar{v}_{d,r}$. For small disk metallicities Z_{disk} , the collision velocity is dominated by the radial drift and is as large as 50 m s^{-1} , while for large $Z_{\text{disk}} > 0.02$, it is dominated by turbulence. The maximum value of the collision velocity due to turbulence is about 30 m s^{-1} , and it decreases with Z_{disk} for $Z_{\text{disk}} > 0.03$. Thus, if the dust particles could survive collisions of 30 m s^{-1} , as suggested by the numerical simulation of collisions of dust aggregates (Wada et al. 2010) and $Z_{\text{disk}} \gtrsim 0.03$, the dust particles would be able to grow without being reduced to small fragments.

6.2. Radial Dependence of the Midplane Dust-to-Gas Ratio

As shown in §4, the turbulence strength and the dust layer structure depend on properties of the gas disk only through $\tilde{\eta}$. For larger $\tilde{\eta}$, the accretion velocity of the dust is faster, and consequently the dust layer is thicker due to stronger turbulence. Figure 11 shows how the midplane dust-to-gas ratio varies with $\tilde{\eta}$. The figure is plotted in the limit of $T_s \ll 1$. For such small particles, f_{mid} is independent of T_s (see Fig. 3). The midplane dust-to-gas ratio f_{mid} decreases with $\tilde{\eta}$ as shown in equation (29). For a gas disk model with a power-law temperature profile, $T \propto r^{-q}$, $\tilde{\eta}$ behaves as $\tilde{\eta} \propto r^{1-q}$. The top axis of Figure 11 indicates corresponding locations in the disk model by Hayashi (1981), i.e., $T = 278(r/\text{AU})^{-1/2}\text{K}$. In a disk with the standard value of the disk metallicity $Z_{\text{disk}} = 0.01$, f_{mid} is less than unity in the most part of the disk except

$r \lesssim 0.1\text{AU}$. In disks with $Z_{\text{disk}} = 0.3$, f_{mid} exceeds 100 for $r \lesssim 1\text{AU}$. We discuss the condition for planetesimal formation through gravitational instability of the dust layer. In a gas disk with a surface density profile $\Sigma_g \propto r^{-p}$, the midplane gas density scales as $\rho_g \propto r^{-p+q/2-3/2}$. The condition that the dust density exceeds the Roche density ($\rho_R \propto r^{-3}$) is $f_{\text{mid}} > \rho_R/\rho_g \propto r^{p-q/2-3/2} \propto r^{p-7/4}$ in a disk model with $q = 1/2$. From the lower line of equation (29), f_{mid} decreases as $f_{\text{mid}} \propto r^{-(1-q)/(2-\delta)} \propto r^{-0.47}$. If $p > 1.3$, the inner part of the disk is more suitable for gravitational instability, and vice versa.

6.3. Does the Liberated Gravitational Energy Go into Turbulence?

In this paper, we calculate the liberated gravitational energy from dust accretion, assuming some fraction of the liberated energy is transferred to turbulence. The estimate of the dust accretion rate is based on the formula for the particle terminal velocity derived in NSH86. “The terminal velocity” means that all the liberated energy is consumed by gas drag, converting directly into the thermal energy of the dust particles and of the surrounding gas molecules. Thus, one may expect that only a small fraction (or nothing) of the liberated energy would be used for maintaining turbulence. However, a comparison with the simulation of KH instability by JHK06 shows that the efficiency factor $C_{\text{eff}} \approx 0.2$ is not negligibly small. In the following subsection, we discuss the validity of using the particle terminal velocity for calculating the energy supply rate to turbulence. The energy liberation rate from the accreting dust calculated in §3 is compared with the deposit rate of the free energy that is the source of several instabilities, such as KH instability and streaming instability.

6.3.1. Kelvin-Helmholtz Instability

The free energy that induces the KH instability originates from the velocity difference between the midplane dust layer and the upper gas layer, and is stored as the dust particles settle to the midplane. We estimate the deposit rate of the free energy during dust sedimentation, and show that it has the same order of magnitude as the energy liberation rate from the dust accretion towards the star. Consider two states of dust distribution: the initial state, in which the dust particles are distributed uniformly in the gas disk, and the final state, in which all the dust has settled at the midplane. In the initial state, there is no vertical shear in the disk, and in the final state, the velocity difference $\Delta v_\theta = \eta v_K$ appears between the midplane dust layer and the upper gas layer. The free energy for KH instability is $\Delta E_{\text{KH}} \sim \frac{1}{2}\Sigma_d \Delta v^2 \sim \frac{1}{2}\Sigma_d \eta^2 v_K^2$, for $\Sigma_d \ll \Sigma_g$. The settling timescale is $\tau_{\text{sed}} = (T_s^2 + 1)/(T_s \Omega_K)$, and then the energy deposit rate is

$$\frac{\Delta E_{\text{KH}}}{\tau_{\text{sed}}} \sim \frac{1}{2}\eta^2 v_K^2 \Omega_K \frac{T_s}{T_s^2 + 1} \Sigma_d, \quad (52)$$

which is the same order as the energy liberation rate of the accreting dust (eqs. [12] and [13]). Hence, the deposition rate of the free energy for KH instability can be estimated by the energy liberation rate of the accreting dust.

6.3.2. Streaming Instability

The free energy for streaming instability originates from the velocity difference between the dust particles and the surrounding gas. When streaming instability begins, the velocity difference decreases as the free energy is consumed by inducing turbulence. In fact, this decrease in the velocity difference can be seen even in the linear growth regime. Youdin & Goodman (2005) showed in their Figure 6 that the velocity difference between the dust and gas decreases (increases) at the locations where the particle density increases (decreases). The spatially averaged value of the free energy decreases as the perturbation grows. Thus, without an energy supply, streaming instability would cease. Given a state in which the velocity difference between the dust and the gas has reduced, the dust particles are no longer in equilibrium: the gravity, the centrifugal force, and the gas drag force are not in balance. The dust particles are accelerated and the velocity difference from the gas rises again. To estimate the effect of the energy deposition on the velocity difference, we consider a state in which the dust density is similar to the gas density, $\rho_d \sim \rho_g$. In such a state, streaming instability occurs efficiently with a growth time of the order of the Keplerian time (for the short wave branch, Youdin & Goodman 2005; Youdin & Johansen 2007). For dust particles of $T_s < 1$, the terminal velocities of the dust and of the gas are of the order of $T_s \eta v_K$ (eq. [9], [10]), and thus, the free energy per unit area is $\Delta E_{\text{str}} \sim \Sigma_d T_s^2 \eta^2 v_K^2$. This deposition of free energy occurs during the acceleration phase of the dust, and thus in the stopping time $T_s \Omega_K^{-1}$, and then the energy is transferred to turbulence in the growth timescale Ω_K^{-1} of streaming instability. Thus, the timescale for the energy deposit in turbulence is the sum of these timescales, and for $T_s \lesssim 1$, $\tau_{\text{str}} = T_s \Omega_K^{-1} + \Omega_K^{-1} \sim \Omega_K^{-1}$. The energy deposition rate is

$$\frac{\Delta E_{\text{str}}}{\tau_{\text{str}}} \sim \eta^2 v_K^2 \Omega_K T_s^2 \Sigma_d, \quad (53)$$

which is smaller by a factor T_s than the estimate from the dust accretion rate (eq.[12]). Hence, our estimate, derived from the dust accretion rate, is appropriate for particles of $T_s \sim 1$. For smaller particles ($T_s \ll 1$), the energy deposition rate is higher for KH instability than for streaming instability, and KH instability is expected to operate first. The energy deposition rate for instability (either for KH or streaming instabilities) is estimated from the energy liberation rate due to dust accretion.

7. SUMMARY

In this paper, we discuss turbulence induced in the dust layer. The turbulence strength or the parameter α is determined using the energetics of dust accretion towards the central star. The key concept is that the dust particles reside in a deeper potential than the gas. The effective potential, including the gas pressure, is $-GM(1 - 2\eta)/r$ for the gas, and $-GM/r$ for the dust.

When angular momentum is transferred from the dust to the gas through gas drag, the dust particles lose more energy than the gas gains. The excess energy can be used for exciting turbulence. If the dust accretion due to gas drag is a primary source of energy liberation, i.e., if the gas accretion rate due to turbulence is much smaller than the dust accretion rate, then the turbulence strength is determined by the energy supply rate from the dust accretion. This is not the case if the gas disk itself is turbulent via, e.g., MRI. If the dust layer is composed of large particles with stopping time $T_s \gg 1$, then the gas accretion may dominate the dust accretion, as discussed in §3.2.

We estimate the dust accretion rate using the terminal velocity profiles of the dust particles in a laminar disk derived by NSH86. The expected turbulence strength and corresponding structure of the dust layer from our analysis agree with the previous analytical result on the marginally KH-unstable dust layer by S98. As our analysis does not assume tight coupling of the dust to the gas, nor specify the mechanism of instability that induces turbulence, it is considered an extension of the analysis of S98 to a more general physical situation of the dust layer. The results of this paper agree with the results in Michikoshi & Inutsuka (2006), which analyzes KH instability of the dust layer composed of particles with large stopping times ($T_s > 1$), as shown in Figure 5.

Our analysis shows that, for particles of $T_s \lesssim 1$, the turbulence strength is smaller than $\alpha_{\text{max}} \sim C_{\text{eff}} \eta T_s$, where $C_{\text{eff}} = 0.19$ is the efficiency of the energy supply to turbulence (see Fig. 2 and eq. [31]). This strength reaches a maximum when the disk metallicity is $Z_{\text{disk}} \sim \sqrt{C_{\text{eff}} \eta} \sim 10^{-2}$. Modifying the disk metallicity from the standard value, 10^{-2} , by any process, results in weaker turbulence and a thinner dust layer, and consequently may accelerate the growth process of the dust particles, as pointed out in S98.

Comparison of our results with previous numerical simulations of KH and streaming instabilities by JHK06 and Bai & Stone (2010) shows quantitative agreement with our analysis for dust particles of $T_s \lesssim 0.1$, although there may be a qualitative disagreement for $T_s \gtrsim 1$ particles (see Figs. 6 – 9). Hence, we conclude that turbulence in the dust layer is controlled by the energy supply from the dust accretion due to gas drag, provided that the dust particles are not so large that $T_s \gtrsim 1$. In such a layer, turbulence strength is estimated by the dust accretion rate (eq.[27]).

This work was stimulated by discussions with Minoru Sekiya. We are grateful to Anders Johansen for providing detailed information on his simulations, and to Chris Ormel and Eugene Chiang for useful discussions. We also thank an anonymous referee for helpful comments. This work was supported in part by Grants-in-Aid for Scientific Research, Nos. 20540232, 22-2942, and 22-7006 from the Ministry of Education, Culture, Sports, Science, and Technology (MEXT), Japan.

APPENDIX

DUST AND GAS VELOCITIES IN STEADY LAMINAR FLOW

We present calculations of the dust and gas velocities in steady laminar flow in this appendix. We follow NSH86, but extend their calculation to the second order of η . The equations of motion of the gas and of the dust are, respectively,

$$\frac{d\mathbf{v}_g}{dt} = -\frac{GM}{r^3}\mathbf{r} - \frac{1}{\rho_g}\nabla P - \frac{\rho_d}{\rho_g}\frac{\Omega_K}{T_s}(\mathbf{v}_g - \mathbf{v}_d), \quad (\text{A1})$$

$$\frac{d\mathbf{v}_d}{dt} = -\frac{GM}{r^3}\mathbf{r} - \frac{\Omega_K}{T_s}(\mathbf{v}_d - \mathbf{v}_g), \quad (\text{A2})$$

where \mathbf{v}_g and \mathbf{v}_d are the velocities of the gas and the dust. The radial and azimuthal components of the velocity in the cylindrical coordinates (r, θ) are normalized by the Keplerian velocity v_K , such as $v_{g,r} = \tilde{v}_{g,r}v_K$, $v_{g,\theta} = \tilde{v}_{g,\theta}v_K$. We assume that the velocities, $v_{g,r}$ etc., vary with r in the same way as the Keplerian velocity v_K , i.e., that the non-dimensional velocities, $\tilde{v}_{g,r}$ etc., are constant with r . This assumption is satisfied when ρ_d/ρ_g and η are constant with r . (see eqs.[A12]-[A19] below) Then, the radial derivative of the velocity is, for example,

$$\frac{\partial}{\partial r}v_{g,r} = -\frac{v_{g,r}}{2r}, \quad (\text{A3})$$

and the radial derivative of other velocity components has a similar form. In a steady axisymmetric state ($\partial/\partial t = \partial/\partial\theta = 0$), equations (A1) and (A2) become

$$-\frac{1}{2}\tilde{v}_{g,r}^2 - \tilde{v}_{g,\theta}^2 = -(1-2\eta) - \frac{\rho_d}{\rho_g}\frac{1}{T_s}(\tilde{v}_{g,r} - \tilde{v}_{d,r}), \quad (\text{A4})$$

$$\frac{1}{2}\tilde{v}_{g,r}\tilde{v}_{g,\theta} = -\frac{\rho_d}{\rho_g}\frac{1}{T_s}(\tilde{v}_{g,\theta} - \tilde{v}_{d,\theta}), \quad (\text{A5})$$

$$-\frac{1}{2}\tilde{v}_{d,r}^2 - \tilde{v}_{d,\theta}^2 = -1 - \frac{1}{T_s}(\tilde{v}_{d,r} - \tilde{v}_{g,r}), \quad (\text{A6})$$

$$\frac{1}{2}\tilde{v}_{d,r}\tilde{v}_{d,\theta} = -\frac{1}{T_s}(\tilde{v}_{d,\theta} - \tilde{v}_{g,\theta}). \quad (\text{A7})$$

The non-dimensional velocities are expanded in a power series of η ,

$$\tilde{v}_{g,r} = \tilde{v}_{g,r,1}\eta + \tilde{v}_{g,r,2}\eta^2 + O(\eta^3), \quad (\text{A8})$$

$$\tilde{v}_{g,\theta} = 1 + \tilde{v}_{g,\theta,1}\eta + \tilde{v}_{g,\theta,2}\eta^2 + O(\eta^3), \quad (\text{A9})$$

$$\tilde{v}_{d,r} = \tilde{v}_{d,r,1}\eta + \tilde{v}_{d,r,2}\eta^2 + O(\eta^3), \quad (\text{A10})$$

$$\tilde{v}_{d,\theta} = 1 + \tilde{v}_{d,\theta,1}\eta + \tilde{v}_{d,\theta,2}\eta^2 + O(\eta^3). \quad (\text{A11})$$

Substituting the above expressions into equations (A4)-(A7) yields in the first order of η ,

$$\tilde{v}_{g,r,1} = \frac{\rho_d}{\rho_g}\frac{2T_s}{T_s^2 + \beta^2}, \quad (\text{A12})$$

$$\tilde{v}_{g,\theta,1} = -\frac{T_s^2 + \beta}{T_s^2 + \beta^2}, \quad (\text{A13})$$

$$\tilde{v}_{d,r,1} = -\frac{2T_s}{T_s^2 + \beta^2}, \quad (\text{A14})$$

$$\tilde{v}_{d,\theta,1} = -\frac{\beta}{T_s^2 + \beta^2}, \quad (\text{A15})$$

which are the same as the results of NSH86. In the second order of η ,

$$\tilde{v}_{g,r,2} = \frac{\rho_d}{\rho_g}\frac{T_s^3(3T_s^2 + 2\beta^2 + 2\beta)}{(T_s^2 + \beta^2)^3}, \quad (\text{A16})$$

$$\tilde{v}_{g,\theta,2} = -\frac{T_s^6 + 3\beta T_s^4 + 3\beta^2 T_s^2 + \beta^4}{2(T_s^2 + \beta^2)^3}, \quad (\text{A17})$$

$$\tilde{v}_{d,r,2} = -\frac{T_s^3(T_s^2 + 2\beta)}{(T_s^2 + \beta^2)^3}, \quad (\text{A18})$$

$$\tilde{v}_{d,\theta,2} = -\frac{\beta(3T_s^4 + 2\beta^2T_s^2 + 3\beta T_s^2 + \beta^3)}{2(T_s^2 + \beta^2)^3} . \quad (\text{A19})$$

ENERGY LIBERATION RATE DUE TO INDIVIDUAL DRAG

In this appendix, we describe a more rigorous derivation of the energy liberation rate due to individual drag than was provided in §3.1. In a laminar disk, the particle drift velocity $v_{d,r}$ calculations were presented in NSH86, to the first order of η . Since the liberated energy is of the second order of η (see eq. [B4] below), we use the particle radial velocity, which is calculated to the order of η^2 in Appendix A,

$$v_{d,r} = -\left[\frac{2T_s}{T_s^2 + \beta^2}\eta + \frac{T_s^3(T_s^2 + 2\beta)}{(T_s^2 + \beta^2)^3}\eta^2 \right] v_K , \quad (\text{B1})$$

where the first term corresponds to equation (2.11) in NSH86. The gas drifts in the opposite direction with the velocity $v_{g,r}$,

$$v_{g,r} = \frac{\rho_d}{\rho_g} \left[\frac{2T_s}{T_s^2 + \beta^2}\eta + \frac{T_s^3(3T_s^2 + 2\beta^2 + 2\beta)}{(T_s^2 + \beta^2)^3}\eta^2 \right] v_K . \quad (\text{B2})$$

The liberated gravitational energy per unit surface area of the disk is,

$$\frac{\partial E_{\text{drag}}}{\partial t} = \frac{1}{2} \int_{-\infty}^{\infty} (\rho_d g_d v_{d,r} + \rho_g g_g v_{g,r}) dz , \quad (\text{B3})$$

where the factor of 1/2 accounts for the work used for the acceleration (and deceleration) of the azimuthal velocity of the dust (and of the gas) as their semi-major axes change. Using equation (B1) and (B2), the energy liberation rate is given by

$$\frac{\partial E_{\text{drag}}}{\partial t} = 2\eta^2 v_K^2 \Omega_K T_s \Sigma_{d,\text{drag}} , \quad (\text{B4})$$

where the effective ‘‘surface density’’ of the dust is

$$\Sigma_{d,\text{drag}} = \frac{\Sigma_d}{\sqrt{\pi}} \int_{-\infty}^{\infty} \frac{\exp(-\tilde{z}^2)}{T_s^2 + \beta^2} \left[1 - \frac{T_s^2}{2(T_s^2 + \beta^2)} \right] d\tilde{z} . \quad (\text{B5})$$

ENERGY LIBERATION RATE DUE TO COLLECTIVE DRAG

In this appendix, we provide a more rigorous derivation of the energy liberation rate due to collective drag than was given in §3.2. The orbital velocity of the gas presented in NSH86 is

$$v_{g,\theta} = \left(1 - \frac{\beta + T_s^2}{\beta^2 + T_s^2} \eta \right) v_K , \quad (\text{C1})$$

where $\beta = (\rho_d + \rho_g)/\rho_g$ varies with the altitude z . The θz component of the Reynolds stress $P_{\theta z}$ due to the turbulent viscosity ν of the gas is

$$P_{\theta z} = (\rho_g + C_{\text{str}}\rho_d)\nu \frac{\partial v_{g,\theta}}{\partial z} . \quad (\text{C2})$$

We add the factor C_{str} to account for the weaker coupling of the dust to the gas for larger dust particles. YL07 has shown that the contribution of the dust to the $r\theta$ -component of the Reynolds stress, $P_{r\theta}$, is a factor $1/(T_s^2 + 1)$ times the gas contribution. From equations (33c) and (B.1) of YL07, it is seen that in both limits of $T_e \ll 1$ and $T_e \gg 1$, $\langle v'_{d,r} v'_{d,\theta} \rangle \sim \langle v'_{g,r} v'_{g,\theta} \rangle T_s^{-2}$ for $T_s \gg 1$, and $\langle v'_{d,r} v'_{d,\theta} \rangle \sim \langle v'_{g,r} v'_{g,\theta} \rangle$ for $T_s \ll 1$, where the prime denotes velocity fluctuations. We assume that a similar relationship holds for the θz -component of the Reynolds stress, $P_{\theta z}$, and thus C_{str} is expressed as⁶

$$C_{\text{str}} = \frac{1}{T_s^2 + 1} , \quad (\text{C3})$$

⁶ Equation (B.1) of YL07 is based on the radial shear effect, and its applicability for the θz -component is not very clear. We simply assume that $P_{r\theta}$ and $P_{\theta z}$ have similar properties. Note also that C_{str} includes only the effect of T_s , assuming that the dust particles act as passive particles in the gas turbulence. This is not the case if the local dust-to-gas ratio is larger than unity. Since the effect of the inertia of the dust on the turbulence is unclear, we

simply adopt equation (C3). For $f_{\text{mid}} \geq 1$, the simple plate drag approximation (eq. [19]) may provide a more accurate estimate. The $\Sigma_{d,\text{vis}}$ estimated from the plate drag approximation (eq. [19]) and from the calculation in this Appendix (eq. [C10]) does not suggest a big difference at large f_{mid} . In the plate drag approximation, $\Sigma_{d,\text{vis}} \propto f_{\text{mid}}^{-1}$, while the calculation in this Appendix gives $\Sigma_{d,\text{vis}} \propto f_{\text{mid}}^{-0.9}$ (see Fig. 1).

This stress transfers angular momentum in the z -direction, and the time derivatives of the angular momentum of the dust and of the gas per unit volume and unit time are, respectively,

$$\frac{\partial l_d}{\partial t} = \frac{C_{\text{str}}\rho_d}{\rho_g + C_{\text{str}}\rho_d} r \frac{\partial P_{\theta z}}{\partial z}, \quad (\text{C4})$$

and

$$\frac{\partial l_g}{\partial t} = \frac{\rho_g}{\rho_g + C_{\text{str}}\rho_d} r \frac{\partial P_{\theta z}}{\partial z}. \quad (\text{C5})$$

Here, we assume that the viscous torque is distributed to the dust and to the gas with the ratio $C_{\text{str}}\rho_d : \rho_g$. The corresponding energy change is $\partial\varepsilon_d/\partial t = \Omega_K \partial l_d/\partial t$ for the dust and $\partial\varepsilon_g/\partial t = \Omega_g \partial l_g/\partial t$ for the gas⁷. In sum, the energy liberation rate per unit area and unit time is

$$\begin{aligned} \frac{\partial E_{\text{vis}}}{\partial t} &= - \int_{-\infty}^{\infty} \left(\frac{\partial\varepsilon_d}{\partial t} + \frac{\partial\varepsilon_g}{\partial t} \right) dz \\ &= -v_K \eta \int_{-\infty}^{\infty} P_{\theta z} \frac{\partial}{\partial z} \left(\frac{1}{1 + C_{\text{str}}(\rho_d/\rho_g)} \right) dz, \end{aligned} \quad (\text{C6})$$

where we use $P_{\theta z}(\pm\infty) = 0$, and the minus sign is added to give the energy release rate. The integration variable is transferred to $\tilde{z} = z/(\sqrt{2}h_d)$, and then using

$$\frac{\partial v_{g,\theta}}{\partial \tilde{z}} = -2f_{\text{mid}}\tilde{z} \exp(-\tilde{z}^2) \frac{\beta^2 + 2\beta T_s^2 - T_s^2}{(T_s^2 + \beta^2)^2} \eta v_K, \quad (\text{C7})$$

and

$$\frac{\partial}{\partial \tilde{z}} \left(\frac{1}{1 + C_{\text{str}}(\rho_d/\rho_g)} \right) = \frac{2C_{\text{str}}f_{\text{mid}}\tilde{z} \exp(-\tilde{z}^2)}{[1 + C_{\text{str}}f_{\text{mid}} \exp(-\tilde{z}^2)]^2}, \quad (\text{C8})$$

equation (C6) becomes

$$\frac{\partial E_{\text{vis}}}{\partial t} = 2\eta^2 v_K^2 \Omega_K T_s \Sigma_{d,\text{vis}}, \quad (\text{C9})$$

where

$$\Sigma_{d,\text{vis}} = \frac{C_{\text{str}}}{\sqrt{\pi}} f_{\text{mid}} \Sigma_d \frac{1 + 2T_s}{1 + T_s} \int_{-\infty}^{\infty} \frac{\beta^2 + 2\beta T_s^2 - T_s^2}{(T_s^2 + \beta^2)^2} \frac{\tilde{z}^2 \exp(-2\tilde{z}^2)}{[1 + C_{\text{str}}f_{\text{mid}} \exp(-\tilde{z}^2)]} d\tilde{z}. \quad (\text{C10})$$

ENERGY DISSIPATION RATE OF TURBULENT DUST MOTION

The energy dissipation rate of the gas in turbulence is

$$\varepsilon_g = \frac{u_{g,\text{eddy}}^2}{\tau_{g,\text{eddy}}}, \quad (\text{D1})$$

where $u_{g,\text{eddy}}$ and $\tau_{g,\text{eddy}}$ are, respectively, the velocity and the turnover time of the largest eddies. Similarly, for the dust,

$$\varepsilon_d = \frac{u_{d,\text{eddy}}^2}{\tau_{d,\text{eddy}}}. \quad (\text{D2})$$

The eddy velocity of the dust, $u_{d,\text{eddy}}$, is estimated from equation (20) of YL07 as

$$u_{d,\text{eddy}}^2 = \frac{u_{g,\text{eddy}}^2}{1 + T_s T_e^{-1} + T_s T_e}, \quad (\text{D3})$$

where $T_e = \tau_{g,\text{eddy}}\Omega_K$ is the non-dimensional turnover time of the gas turbulence. The turnover time of the dust turbulence, $\tau_{d,\text{eddy}}$, is estimated as the larger value of $\tau_{g,\text{eddy}}$ and τ_{stop} , i.e.,

$$\tau_{d,\text{eddy}} = \max(\tau_{g,\text{eddy}}, \tau_{\text{stop}}). \quad (\text{D4})$$

From equations (D1)-(D4),

$$\varepsilon_d = C_{\text{ene}} \varepsilon_g, \quad (\text{D5})$$

⁷ We assume that the rotational velocities of the dust and the gas are Ω_K and Ω_g respectively, neglecting the modification of the rotational velocity due to gas drag. This assumption is justified if $f_{\text{mid}} \geq 1$ and if the angular momentum exchange occurs between

the dust-dominant layer (rotating with Ω_K) and the gas-dominant layer (rotating with Ω_g). For $f_{\text{mid}} \leq 1$, the energy liberation due to collective drag is neglected compared to that due to individual drag (see Fig. 1).

where C_{ene} is approximately

$$C_{\text{ene}} = \begin{cases} \frac{1}{T_s T_e + 1} & \text{for } T_s \leq T_e \\ \frac{1}{T_s^2 (T_e^{-2} + 1)} & \text{for } T_s > T_e \end{cases} \quad (\text{D6})$$

REFERENCES

- Bai, X.-N., & Stone, J. M. 2010a, *ApJ*, 722, 1437
 Bai, X.-N., & Stone, J. M. 2010b, *ApJ*, 722, L220
 Barranco, J. A. 2009, *ApJ*, 691, 907
 Brauer, F., Dullemond, C. P., Johansen, A., Henning, Th., Klahr, H., & Natta, A. 2007, *ApJ*, 469, 1169
 Carballido, A., Bai, X.-N., & Cuzzi, J. N. 2011, *MNRAS*, online early
 Carballido, A., Cuzzi, J. N., & Hogan, R. C. 2010, *MNRAS*, 405, 2339
 Carballido, A., Fromang, S., & Papaloizou, J. 2006, *MNRAS*, 373, 1633
 Carballido, A., Stone, J. M., & Turner, N. J. 2008, *MNRAS*, 386, 145
 Chandrasekhar S. 1961, *Hydrodynamic and Hydromagnetic Stability* (New York:Dover Publications, Inc.)
 Champney, J. M., Dobrovolskis, A. R., & Cuzzi, J. N., 1995, *Physics of Fluids*, 7, 1703
 Chiang, E., & Youdin, A. N. 2010, *Annual Review of Earth and Planetary Sciences*, 38, 493
 Cuzzi, J. N., Dobrovolskis, A.R., & Champney, J. M. 1993, *Icarus*, 106, 102
 Cuzzi, J. N., Hogan, R. C., Paque, J. M., & Dobrovolskis, A. R. 2001, *ApJ*, 546, 496
 Dobrovolskis, A.R., Dacles-Mariani, J. S., & Cuzzi, J. N. 1999, *J. Geophys. Res.*, 104, 30805
 Fleming, T., Stone, J. M. 2003, *ApJ*, 585, 908
 Fromang, S., & Nelson, R. P. 2009, *A&A*, 496, 597
 Fromang, S., & Papaloizou, J. 2006, *A&A*, 452, 751
 Gammie, C. F. 1996, *ApJ*, 457, 355
 Garaud, P., & Lin, D. N. C. 2004, *ApJ*, 608, 1050
 Goldreich, P., & Ward, W. R. 1973, *ApJ*, 183, 1051
 Gómez, G. C., & Ostriker, E. C. 2005, *ApJ*, 630, 1093
 Goodman, J., & Pindor, B. 2000, *Icarus*, 148, 537
 Hayashi, C. 1981, *Prog. Theor. Phys. Suppl.*, 70, 35
 Ishitsu, N., & Sekiya, M. 2002, *Earth, Planets and Space*, 54, 917
 Ishitsu, N., & Sekiya, M. 2003, *Icarus*, 165, 181
 Johansen, A., Henning, Th., & Klahr, H. 2006, *ApJ*, 643, 1219 (JHK06)
 Johansen, A., & Klahr, H. 2005, *ApJ*, 634, 1353
 Johansen, A., & Klahr, H., & Henning, Th. 2011, *A&A*, 529, id.A62
 Johansen, A., Oishi, J. S., Mac Low, M.-M., Klahr, H., Henning, T., & Youdin, A. 2007, *Nature*, 448, 1022
 Johansen, A., & Youdin, A. 2007, *ApJ*, 662, 627
 Lee, A. T., Chiang, E., Asay-Davis, X., & Barranco, J. 2010, *ApJ*, 718, 1367
 Lesur, G., & Ogilvie, G. I. 2010, *MNRAS*, 404, L64
 Lyra, W., Johansen, A., Klahr, H., & Piskunov, N., *A&A*, 491, L41
 Lyra, W., Johansen, A., Zsom, A., Klahr, H., & Piskunov, A&A, 497, 869
 Michikoshi, S., & Inutsuka, S.-I. 2006, *ApJ*, 641, 1131
 Nakagawa, Y., Sekiya, M., & Hayashi, C. 1986, *Icarus*, 67, 375 (NSH86)
 Okuzumi, S., & Hirose, S. 2011, *ApJ*, submitted
 Ormel, C. W., & Cuzzi, J. N. 2007, *A&A*, 466, 413
 Press, W. H., Flannery, B. P., Teukolsky, S. A., & Vetterling, W. T. 1992, *Numerical Recipes in Fortran* (Cambridge University Press)
 Sano, T., Miyama, S. M., Umebayashi, T., & Nakano, T. 2000, *ApJ*, 543, 486
 Sekiya, M. 1983, *Prog. Theor. Phys.*, 69, 1116
 Sekiya, M. 1998, *Icarus*, 133, 298 (S98)
 Sekiya, M., & Ishitsu, N. 2000, *Earth, Planets and Space*, 52, 517
 Sekiya, M., & Ishitsu, N. 2001, *Earth, Planets and Space*, 53, 761
 Stone, J. M., & Balbus, S. A. 1996, *ApJ*, 464, 364
 Suzuki, T. K., Muto, T., & Inutsuka, S.-I. 2010, *ApJ*, 718, 1289
 Takeuchi, T., & Lin, D. N. C. 2002, *ApJ*, 581, 1344
 Turner, N. J., Willacy, K., Bryden, G., & Yorke, H. W. 2006, *ApJ*, 639, 1218
 Wada, K., Tanaka, H., Suyama, T., Kimura, H., & Yamamoto, T. 2009, *ApJ*, 702, 1490
 Weidenschilling, S. J. 2003, *Icarus*, 165, 438
 Weidenschilling, S. J. 2006, *Icarus*, 181, 572
 Weidenschilling, S. J. 2010, *Meteoritics and Planetary Science*, 45, 276
 Youdin, A. N., & Chiang, E. I. 2004, *ApJ*, 601, 1109
 Youdin, A. N., & Goodman, J. 2005, *ApJ*, 620, 459
 Youdin, A., & Johansen, A. 2007, *ApJ*, 662, 613
 Youdin, A. N., & Lithwick, Y. 2007, *Icarus*, 192, 588 (YL07)